INTERNATIONAL JOURNAL FOR NUMERICAL METHODS IN FLUIDS
Int. J. Numer. Meth. Fluids **26**: 1055–1084 (1998)

APPLICATION OF A RANGE OF TURBULENCE ENERGY MODELS TO THE COMPUTATION OF THE INTERNAL TIDE

JIUXING XING AND ALAN M. DAVIES*

Proudman Oceanographic Laboratory, Bidston Observatory, Birkenhead, Merseyside L43 7RA, UK

SUMMARY

A non-linear, three dimensional, baroclinic model with a range of turbulence energy submodels and algebraic models for the vertical mixing of momentum and density, is used in a cross shelf form to examine the spatial variation of vertical mixing due to the internal tide at the shelf edge off the west coast of Scotland. Particular emphasis is placed on the sensitivity of the mixing to the form of the parameterization of the subgrid scale processes. Calculations using a fine finite difference grid in the horizontal of the order of 0.6 km with 50 sigma levels in the vertical and a typical winter time stratification, show that the model can reproduce the major features of the internal tide with the range of parameterizations considered here, although there are some differences in the magnitude of both the velocity and mixing intensity of the internal tide, depending upon the parameterization of the mixing. In particular, the turbulence energy models show regions of intense mixing at the sea bed where the internal tide is generated and at the sea surface above the shelf break associated with the shear production of turbulence. These differences suggest that detailed measurements of current, internal displacement of density fields and turbulence dissipation rate may be able to assess the accuracy of the various mixing models. Calculations, however, show that the internal tide is particularly sensitive to small perturbations in the initial density field, suggesting that besides detailed measurements to validate the model, a detailed synoptic data set is required for model initialization. © 1998 John Wiley & Sons, Ltd.

KEY WORDS: internal tides; shelf edge; stratification; turbulence energy; baroclinic; eddy viscosity

1. INTRODUCTION

For tides in homogenous regions, the problem of the sensitivity of tidal current profiles and turbulent mixing to the form of the turbulence energy submodel used to parameterize subgrid scale mixing, has been considered previously [1–6].

Initial calculations were performed using a three-dimensional model covering the European continental shelf [1] with a no-slip condition at the sea bed; a prognostic equation for turbulence energy and the mixing length which was determined diagnostically using Blackadar's [7] form of the mixing length. A comparison of tidal current profiles computed using this model with those derived using a simple flow dependent viscosity [8,9] and with observations [1] did not reveal any significant improvement in the accuracy of the model, except possibly in the near bed region, arising from the use of a no-slip rather than a slip condition.

* Correspondence to: Proudman Oceanographic Laboratory, Bidston Observatory, Birkenhead, Merseyside L43 7RA, UK.

CCC 0271–2091/98/091055–30$17.50

Received July 1996
Revised April 1997

In a subsequent series of calculations, a high resolution limited area model of the Irish Sea with both no-slip [4] and slip conditions [6], with a range of turbulence energy models from a single prognostic turbulence model with an algebraic mixing length to a two-equation prognostic model ($q^2 - q^2\ell$ model, defined later) for both turbulence energy and mixing length were used to study both the M_2 tide and its higher harmonic.

Computed tidal current profiles were compared with observations and with earlier models which used a flow related viscosity and both no-slip [10] and slip boundary conditions, with particular emphasis on the higher harmonics [11]. However, there was no improvement in the accuracy of the turbulence models compared with the simple flow related viscosity formulations. Indeed, in a comparison of a flow related viscosity model, with shear dependent viscosity models, and a two-equation turbulence ($k - \epsilon$) model, Davies and Gerritsen [3] found that the $k - \epsilon$ model was the least accurate.

For tides in homogeneous sea regions, calculations showed that there was little difference in tidal current profiles or computed eddy viscosity values derived using a range of turbulence energy models in both shallow or deep [4,5] areas. Some slight differences were evident in the case of a stratified shallow sea region [12], although a highly accurate series of measurements would be required to distinguish between the models. However, in deep water, calculations of the internal tide in the shelf break region using a two-equation turbulence energy model ($q^2 - q^2\ell$ model) [13,14] have shown the importance of an accurate description of the density field, hence the role of internal mixing in determining the density distribution. This suggests that the intensity and spatial variability of the internal tide and the associated mixing may be particularly sensitive to the parameterization of mixing.

In this paper, the sensitivity of the internal tide and the associated mixing to the parameterization of the subgrid scale mixing processes was examined, using a range of turbulence energy models to represent the internal tidal mixing. The region chosen for the investigation is the shelf edge area off the west coast of Scotland, where there is a strong internal tide [15,16] and detailed measurements will be made in the future.

The internal tide is generated when stratification intersects a topographic feature, such as the shelf edge [17–22]. During the tidal cycle the movement of the stratification against the topography gives rise to an internal tide. The magnitude of the internal displacement of the density field produced by the internal tides [16] is large and can generate intense mixing regions [23,24,13,14].

In this paper, a three-dimensional hydrodynamic model with a time evolving density field is used to consider the influence of the parameterization of subgrid scale mixing upon the magnitude and spatial distribution of the internal tide in the shelf edge region off the west coast of Scotland. The model used here is based upon that described by Xing and Davies [13,14], and a detailed set of numerical calculations were carried out to determine its accuracy by comparison with the analytical solutions published by Craig [19]. Although the solutions of Craig [19] are inviscid, linear and restricted to a shelf edge of constant slope, analytical solutions are available for both subcritical and supercritical internal tides. These solutions were used to test the accuracy of the present model for a range of horizontal and vertical grid spacings, values of horizontal diffusion and the use of a central differencing, or total variation diminishing (TVD) scheme for density advection. The results of these calculations showed that provided the order of 50 sigma levels was used in the vertical, together with a fine finite difference grid (of order 0.6 km) in the horizontal, with a minimum value of horizontal diffusion (of order 5 $m^2\ s^{-1}$) then the analytical solutions of Craig [19] could be reproduced. Although the solutions of Craig [19] were for an inviscid set of equations, in the numerical solutions it was necessary to include a small horizontal diffusion for numerical stability, which

did not affect the accuracy provided it was kept to a minimum (of order 5 $m^2\ s^{-1}$ with the horizontal grid of order 0.6 km). Also, for weak vertical stratification, modest slopes and small tidal amplitude, there were no significant differences between solutions computed using central differencing and the TVD scheme for density advection. However, for strong stratification, steep slope and strong tidal forcing, an accurate solution could only be obtained using the TVD method [14]. In this paper the model is extended to include a range of parameterizations of vertical mixing processes and an extensive series of calculations is performed to examine the effects of each upon the internal tide. The greatest spatial variability occurs in the cross shelf direction, so the three-dimensional model in its cross shelf form is used.

A brief description of the three-dimensional hydrodynamic model is presented in Section 2 (the reader is referred to References [13,14] for more detail), with Section 3 describing the range of parameterizations of vertical mixing used in the model. Results from the comparison of the internal tide generation produced using this range of mixing processes is presented in the latter part of the paper.

2. THE HYDRODYNAMIC MODEL

The full three-dimensional equations in polar co-ordinates used in the model are given by

$$\frac{\partial \zeta}{\partial t}+\frac{1}{R\cos\phi}\left(\frac{\partial}{\partial \chi}\int_{-h}^{\zeta} u\,\mathrm{d}z+\frac{\partial}{\partial \phi}\int_{-h}^{\zeta} v\cos\phi\,\mathrm{d}z\right)=0, \tag{1}$$

$$\frac{\partial u}{\partial t}-\gamma v+\mathrm{Add}_u+\mathrm{Diff}_u=\frac{-g}{\rho_0 R\cos\phi}\frac{\partial P}{\partial \chi}+\frac{\partial}{\partial z}\left(A_\mathrm{v}\frac{\partial u}{\partial z}\right), \tag{2}$$

$$\frac{\partial v}{\partial t}+\gamma u+\mathrm{Add}_v+\mathrm{Diff}_v=\frac{-g}{\rho_0 R}\frac{\partial P}{\partial \phi}+\frac{\partial}{\partial z}\left(A_\mathrm{v}\frac{\partial v}{\partial z}\right), \tag{3}$$

with

$$\mathrm{Add}_u=\frac{u}{R\cos\phi}\frac{\partial u}{\partial \chi}+\frac{v}{R}\frac{\partial u}{\partial \phi}+w\frac{\partial u}{\partial z}-u\frac{v\tan\phi}{R}, \tag{4a}$$

$$\mathrm{Add}_v=\frac{u}{R\cos\phi}\frac{\partial v}{\partial \chi}+\frac{v}{R}\frac{\partial v}{\partial \phi}+w\frac{\partial v}{\partial z}+\frac{u^2\tan\phi}{R}, \tag{4b}$$

$$\mathrm{Diff}_u=-\frac{A_\mathrm{h}}{R^2}\left[\frac{1}{\cos^2\phi}\frac{\partial^2 u}{\partial \chi^2}-\tan\phi\frac{\partial u}{\partial \phi}+\frac{\partial^2 u}{\partial \phi^2}\right], \tag{5a}$$

$$\mathrm{Diff}_v=-\frac{A_\mathrm{h}}{R^2}\left[\frac{1}{\cos^2\phi}\frac{\partial^2 v}{\partial \chi^2}-\tan\phi\frac{\partial v}{\partial \phi}+\frac{\partial^2 v}{\partial \phi^2}\right], \tag{5b}$$

where Add_u, Add_v and Diff_u and Diff_v are the advective and diffusion terms, with the vertical velocity w given by

$$w=\frac{1}{R\cos\phi}\frac{\partial}{\partial \chi}\int_z^{\zeta} u\,\mathrm{d}z-\frac{\tan\phi}{R}\int_z^{\zeta} v\,\mathrm{d}z+\frac{1}{R}\frac{\partial}{\partial \phi}\int_z^{\zeta} v\,\mathrm{d}z, \tag{6}$$

with the pressure P at any depth z given by

$$P=g\rho_0\zeta+g\int_0^z \rho(z)\,\mathrm{d}z. \tag{7}$$

In these equations A_v, A_h are vertical and horizontal viscosity.

In addition to these equations, the model also contains prognostic equations describing the advection of a conservative variable θ, which can be density, temperature, salinity or any other conservative tracer, of the form

$$\frac{\partial \theta}{\partial t} + \mathrm{Add}_\theta + \mathrm{Diff}_\theta = \frac{\partial}{\partial z}\left(K_v \frac{\partial \theta}{\partial z}\right), \tag{8}$$

where K_v is the vertical diffusion coefficient for θ, with Add_θ and Diff_θ the horizontal advection and diffusion of θ.

In these equations, u, v are the east (χ) and north (ϕ) components of velocity, ζ is the free surface elevation, z is the vertical co-ordinate, t is time and h is the water depth. The Coriolis parameter is denoted by γ, g is acceleration due to gravity, R is the radius of the earth with ρ_0 mean density and $\rho(z)$ deviations from the mean.

In an initial series of calculations an idealized shelf edge topography (Figure 1) was used. In this model the along shelf pressure gradient term $\partial P/\partial \phi$ is taken as zero, and the model is forced at the offshore open boundary. A condition of no flow normal to the coast is assumed at land boundaries. Real shelf edge topography off the west coast of Scotland and initial temperature fields approximating those measured by Ellett *et al.* [25] were used in the range of calculations described later. A simple equation of state [26] to convert temperature into density, namely

$$\rho = \rho_0[1 - \alpha(T - T_0)], \tag{9}$$

with $\alpha = 0.0002/°\mathrm{C}$ and T_o a reference temperature corresponding to ρ_0 is applied to the calculation. At sea surface and sea bed, the vertical derivative of temperature was set equal to zero. A zero normal derivative condition was used for the current at the sea surface (i.e. there was no external stress), with a slip condition applied at the sea bed, thus

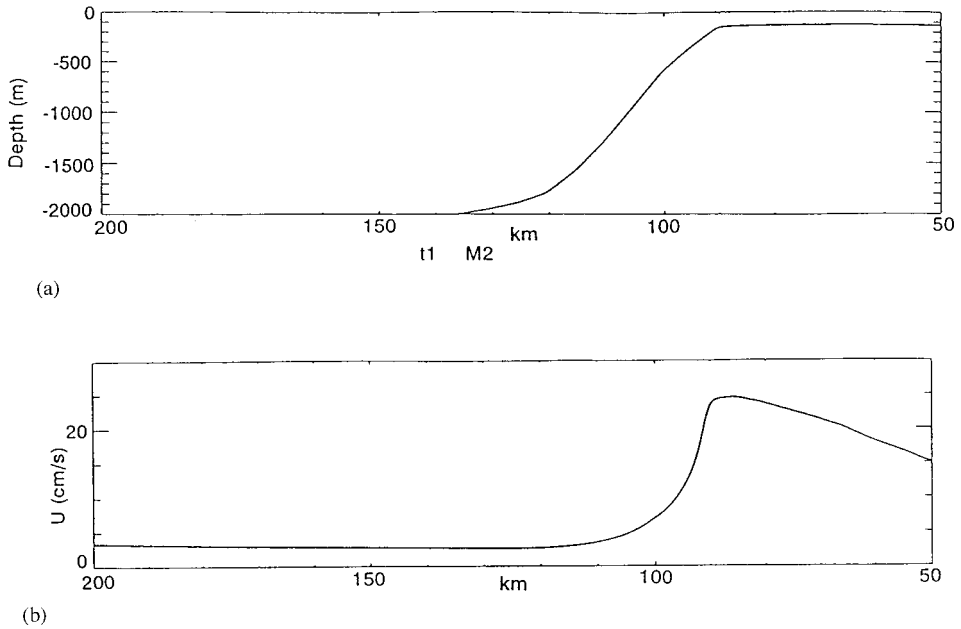

Figure 1. Cross section variation of (a) water depths (m) and (b) barotropic M_2 tidal current (cm s^{-1}).

$$-\rho A_v \frac{\partial u}{\partial z} = k\rho u_h (u_h^2 + v_h^2)^{1/2}, \qquad -\rho A_v \frac{\partial v}{\partial z} = k\rho v_h (u_h^2 + v_h^2)^{1/2}, \tag{10}$$

with u_h, v_h the components of the bed currents.

The solution of these hydrodynamic equations is found using a normalized sigma co-ordinate $\sigma = (z + \zeta)/(h + \zeta)$ in the vertical. (Significant care must be taken with the internal pressure gradients in sigma co-ordinates e.g. References [27–29] and details are given in References [13,14]). Numerical discretization was accomplished using the Arakawa C grid in the horizontal, and in the vertical the two components of velocity are computed at the same point, although this is staggered with respect to the density points. In a previous series of calculations [13,14] a grid spacing of 1/96° (of order 0.6 km) in the horizontal, with 50 levels in the vertical on an irregular grid giving enhanced resolution in the near bed region, was found to give an accurate solution (see discussion in Introduction). The same grid is used in the calculations carried out here.

Discretization in time is accomplished using a time splitting method in which the current is expressed in terms of its depth mean part and a deviation from the mean. The vertical diffusion terms for momentum and temperature were time centred (an implicit algorithm) and therefore did not impose a restriction on the time step. The advection of momentum was integrated using a time split method with central differencing in the horizontal, with a time step below that determined by the grid spacing and advection velocity. The TVD scheme used here is described in detail (with an associated set of references) by James [30]. It is based upon a combination of first-order upwind and Lax–Wendroff schemes and a Superbee limiter (see Reference [30] for details). The TVD method is particularly accurate [31] in advecting sharp density gradients over steep topography and was used for advection in the density equation, although momentum advection was accomplished using central differencing. (A comparison of the accuracy of the TVD scheme and central differencing is given in Reference [14]).

3. PARAMETERIZATION OF SUBGRID SCALE VERTICAL MIXING

One of the aims of the present paper is to examine the intensity and spatial/temporal variability of the turbulence associated with internal tides, and the sensitivity of the mixing and internal tidal current structure to the parameterization of mixing. Therefore, a number of very different mixing models are considered. (An indication of the range of models at present used in oceanography is given in References [32–37] and will not be reviewed here).

3.1. Two prognostic equation model (the $q^2 - q^2\ell$ model)

This model was used by Xing and Davies [4–6] to examine the M_2 barotropic tide in the Irish Sea and on the shelf edge region off the west coast of Scotland, hence it is interesting to use the same model again in stratified conditions. This model involves two prognostic equations, one for $q^2 = 2E$, (where E is turbulence energy), namely

$$\frac{\partial q^2}{\partial t} + \mathrm{Add}_q + \mathrm{Diff}_q = 2A_v \left\{ \left(\frac{\partial u}{\partial z} \right)^2 + \left(\frac{\partial v}{\partial z} \right)^2 \right\} + \frac{\partial}{\partial z} \left\{ S_q q \ell \frac{\partial q^2}{\partial z} \right\} - 2 \frac{q^3}{B_1 \ell} + 2G, \tag{11}$$

with $G = -K_v(\partial b/\partial z)$, accounting for the suppression of turbulence by buoyancy, where $b = -g(\rho - \rho_0)/\rho_0$ is buoyancy, ρ is the density and ρ_0 a background average density, K_v is a diffusion coefficient for density, and Add_q, Diff_q the horizontal advection and diffusion of turbulence. A horizontal diffusion coefficient of 5 $m^2\ s^{-1}$ was used in all calculations. This

value prevents an accumulation of energy at the grid scale due to the non-linear terms but is not sufficiently large to artificially smooth the physically realistic and resolvable part of the solution (see Xing and Davies [13,14], who compared results with analytical solutions of Craig [19]).

The equation for the mixing length, takes the form,

$$\frac{\partial}{\partial t}(q^2\ell) + \mathrm{Add}_e + \mathrm{Diff}_e = \ell E_1 A_\mathrm{v}\left\{\left(\frac{\partial u}{\partial z}\right)^2 + \left(\frac{\partial v}{\partial z}\right)^2\right\} + \frac{\partial}{\partial z}\left\{S_q q\ell \frac{\partial}{\partial z}(q^2\ell)\right\} - \frac{q^3}{B_1} W + \ell E_1 G, \tag{12}$$

where $S_q = 0.2$, $B_1 = 16.6$ and $E_1 = 1.8$ are specified constants, with W a wall proximity function (see Reference [34], for details). The horizontal advection and diffusion terms for $q^2\ell$ are given by Add_e and Diff_e, respectively.

The diffusion coefficients for momentum A_v and density K_v in a stratified fluid are computed using the following equation,

$$A_\mathrm{v} = \ell q S_M, \qquad K_\mathrm{v} = \ell q S_H, \tag{13}$$

with S_M and S_H given by the algebraic expressions (see Reference [35] for the form of these expressions).

3.2. *One prognostic equation model (k–ℓ model)*

In this model, the eddy viscosity A_v and eddy diffusivity K_v are computed from the turbulence energy E, derived from a single prognostic equation, and the mixing length l is determined here in an algebraic manner (see below).

The turbulence energy E is computed from

$$\frac{\partial E}{\partial t} = A_\mathrm{v}\left\{\left(\frac{\partial u}{\partial z}\right)^2 + \left(\frac{\partial v}{\partial z}\right)^2\right\} + \beta_0 \frac{\partial}{\partial z}\left(A_\mathrm{v}\frac{\partial E}{\partial z}\right) + G - \epsilon, \tag{14}$$

where the turbulence dissipation ϵ is given by

$$\epsilon = C_0 C_1 E^2 / A_\mathrm{v}, \tag{15}$$

with

$$A_\mathrm{v} = C_0 \ell_\mu E^{1/2} \quad \text{and} \quad K_\mathrm{v} = C_0 \ell_\lambda E^{1/2}, \tag{16}$$

where $\beta_0 = 0.73$, $C_0 = C^{1/4}$, $C_1 = C_0^3$ where $C = 0.046$ [38]. In these equations, ℓ_μ and ℓ_λ are the mixing lengths for momentum and diffusion, given by

$$\ell_\mu = \psi_\mu \ell_0 \quad \text{and} \quad \ell_\lambda = \psi_\lambda \ell_0, \tag{17}$$

where ψ_μ and ψ_λ are appropriate stability functions for viscosity and diffusivity (the form of which is discussed in the next section), and ℓ_0 is the mixing length in homogeneous conditions.

The mixing length ℓ_0 can be determined either in terms of an integral of the turbulence energy [7,9,1,39,36] or using an algebraic expression. A simple algebraic form of the mixing length (Johns and Xing [40], referred to later as the JX mixing length) which has been used in a number of tidal calculations [5,6] is given by

$$\ell_0 = 1/\left(\frac{1}{\ell_1} + \frac{1}{\ell_2}\right), \tag{18}$$

with

$$\ell_1 = K(\sigma H + z_0)\exp(\beta_1 \sigma), \tag{19}$$

and

$$\ell_2 = K(H - \sigma H + z_s), \tag{20}$$

where $K = 0.4$ is Von Karman's constant, β_1 is an empirical coefficient, $H = h + \zeta$ is the total depth of water, σ is the normalized vertical co-ordinate, with z_0 the bed roughness length, and z_s a surface roughness length, which controls the value of ℓ at the sea surface.

In a turbulence energy submodel for tidal flows the vertical flux of turbulence energy or $q^2\ell$ is zero at the sea surface. The vertical flux through the sea bed is also zero if a no-slip condition is applied at the bed. With a slip condition at the bed, the sea bed turbulence energy E_{bed} given by $E_{\text{bed}} = U_*^2/C_b^{1/2}$, with C_b an empirical coefficient, and U_* the friction velocity.

3.3. A Richardson number dependent viscosity (R_i model)

An alternative to applying a turbulence energy model is to compute the eddy viscosity and diffusivity as a function of the Richardson number, thus

$$A_v = A_1\psi_\mu(z) + A_0,$$
$$K_v = B_1\psi_\lambda(z) + B_0, \tag{21}$$

where A_0, B_0 are the constant background eddy viscosity or diffusivity, with A_1, B_1, either constant or a function of the flow field. A formulation used by Naimie *et al.* [41] in studying flow around Georges Bank was to relate A_1 to the depth mean current u, v, using a formulation given by Davies [8], namely

$$A_1 = \frac{K_a(\bar{u}^2 + \bar{v}^2)}{\omega}, \tag{22}$$

with $K_a = 2.0 \times 10^{-5}$ a constant and $\omega = 1.0 \times 10^{-4}\ \text{s}^{-1}$ a typical frequency. The function $\psi_\mu(z)$, $\psi_\lambda(z)$, determining the profile of viscosity/diffusivity through the vertical is taken as a function of the Richardson number, thus [42]

$$\psi_\mu(z) = \frac{1}{(1 + 10R_i)^{1/2}} \qquad \psi_\lambda(z) = \frac{1}{(1 + 3.33R_i)^{1.5}}, \tag{23}$$

where

$$R_i = \frac{-g(\partial\rho/\partial z)}{\rho_0[(\partial u/\partial z)^2 + (\partial v/\partial z)^2]}. \tag{24}$$

In the calculations described subsequently we use $A_1 = 0.005\ \text{m}^2\ \text{s}^{-1}$, $A_0 = 0.0005\ \text{m}^2\ \text{s}^{-1}$ and $B_1 = 0.005\ \text{m}^2\ \text{s}^{-1}$, with $B_0 = 1.4 \times 10^{-6}\ \text{m}^2\ \text{s}^{-1}$ representing molecular diffusion.

3.4. Simplified stability function

An alternative to specifying different stability functions for ψ_μ and ψ_λ is to use the same stability function for both [33], of the form

$$\psi_\mu = \psi_\lambda = \psi = \frac{1}{(R_i + (R_i^2 + 1)^{1/2})^2}. \tag{25}$$

Table 1. Summary of calculations

Calculation	Calculation	Stability functions
(a) Sensitivity to parameterization of vertical diffusion		
1	$q^2-q^2\ell$	S_H, S_M
2	k–ℓ	$\psi_\mu = \psi_\lambda = 1$
3	k–ℓ	S_H, S_M
4	k–ℓ	$\ell = \ell_0 f(R_i)$
5	k–ℓ	$\psi_\mu = f_1(R_i)$, $\psi_\lambda = f_2(R_i)$
6	Eddy coefficient	Richardson number dependent
(b) Sensitivity to density field		
Calculation	Density field	
7	Summer	
8	Perturbed winter	
9	Perturbed summer	

Calculations using the range of mixing length formulations presented here will be described subsequently.

4. INFLUENCE OF VERTICAL MIXING ON THE INTERNAL TIDE

4.1. Introduction

In the series of calculations presented here, a slip condition was applied at the sea bed with $z_0 = 0.005$ m a typical bottom roughness value. Since we are primarily concerned with the influence of the parameterization of mixing and changes in stratification, we will assume a spatially constant z_0 and use this value in all calculations. By applying a slip condition at the sea bed, the hydrodynamic equations can be integrated using a time splitting approach (see References [4–6] for details).

4.2. The $q^2 - q^2\ell$ model

In the first calculation (Calculation 1, Table 1) the initial temperature field corresponding to an observed winter situation [25] was used. The temperature profile and the corresponding profile of the Brunt–Vaisala frequency N^2, which reaches a maximum at about 50 m below the surface are given in Figure 2. The two-equation turbulence energy submodel, Equations (11) and (12), was used to compute q^2 and the mixing length ℓ, with eddy viscosity and diffusivity determined from Equation (13). It should be noted that because of differences in the stability functions S_M and S_H, eddy viscosity and diffusivity have different values in this calculation. Motion in the model was started from the specified density field shown in Figure 2, with M_2 tidal forcing, and integrated in time for 30 tidal cycles before being harmonically analysed. Diffusion is included, so some diffusion of the density field will occur during this time which will change the density field and thus the internal tide.

Contours of the amplitude of the u component of the internal tidal current at the top of the shelf slope, where the internal tide is largest at the M_2 frequency and its higher harmonic namely M_4 are given in Figure 3(a(i)(ii)). (The currents shown here are due to the internal tide, with the total tidal current obtained by the addition of the depth mean tidal current induced by the surface tidal forcing (the barotropic tide) to these values). The process influencing the internal tidal current shown here is predominantly the internal pressure gradients, produced by the internal displacement of the density field generated by the internal tide. A secondary process is the retardation of the flow by bottom friction, which produces bottom turbulence and hence enhanced mixing in regions of strong bottom current. This mixing is reduced significantly by stratification effects in the upper part of the water column, although increased mixing can occur here owing to shear produced by the internal tide.

It is evident from Figure 3(a(i)) and the contours of internal displacement Figure 3(b(i)) that the u component of the M_2 internal tidal current gives rise to a region of strong (tidal amplitude of order 20 cm s^{-1}) near bed currents near the top of the shelf slope (located about 95 km offshore, Figure 3(a(i))). The amplitude of the M_2 tidal current at this location initially decreases with height above the bed, although an increase in tidal current magnitude is clearly evident in the near surface layer, with an associated phase change of 180° in the vertical. Regions of intensified surface M_2 tidal currents about 88 km offshore are clearly evident in Figure 3(a(i)), with an area of increased M_2 tidal current magnitude extending from the location of the maximum bed tidal current into the ocean (Figure 3(a(i))). The location of the maximum tidal current amplitude corresponds to the ray paths of the propagation of the internal tide [23].

The on-shelf propagation of internal tidal energy gives rise to second mode internal tides on the shelf with an associated 180° phase change, and a spatial distribution showing regions of alternating stronger (of order 8 cm s^{-1}) and weaker (of order 4 cm s^{-1}) near bed internal tidal currents.

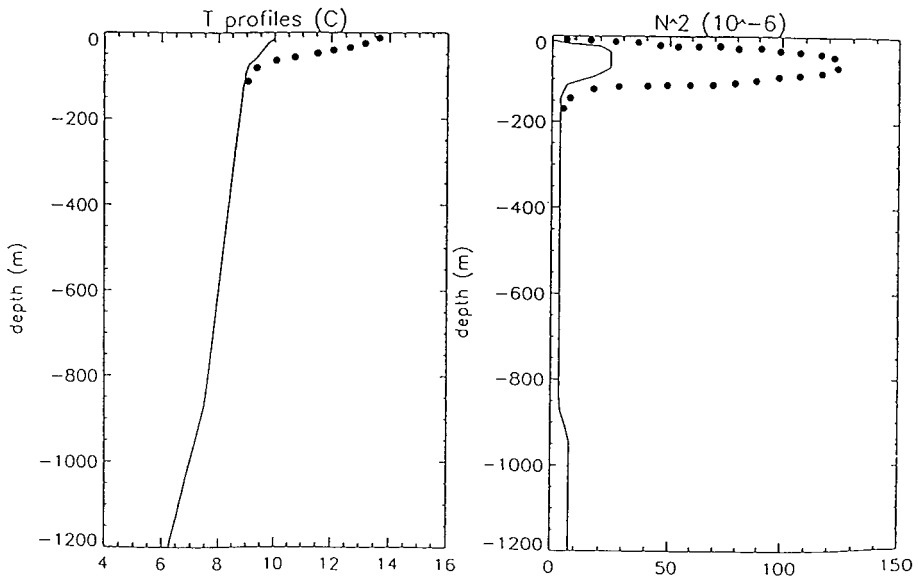

Figure 2. Profiles of temperature T (°C) and Brunt–Vaisala frequency $N^2 \times 10^{-6}$ (s^{-2}) for winter (solid) and summer (dotted) stratification.

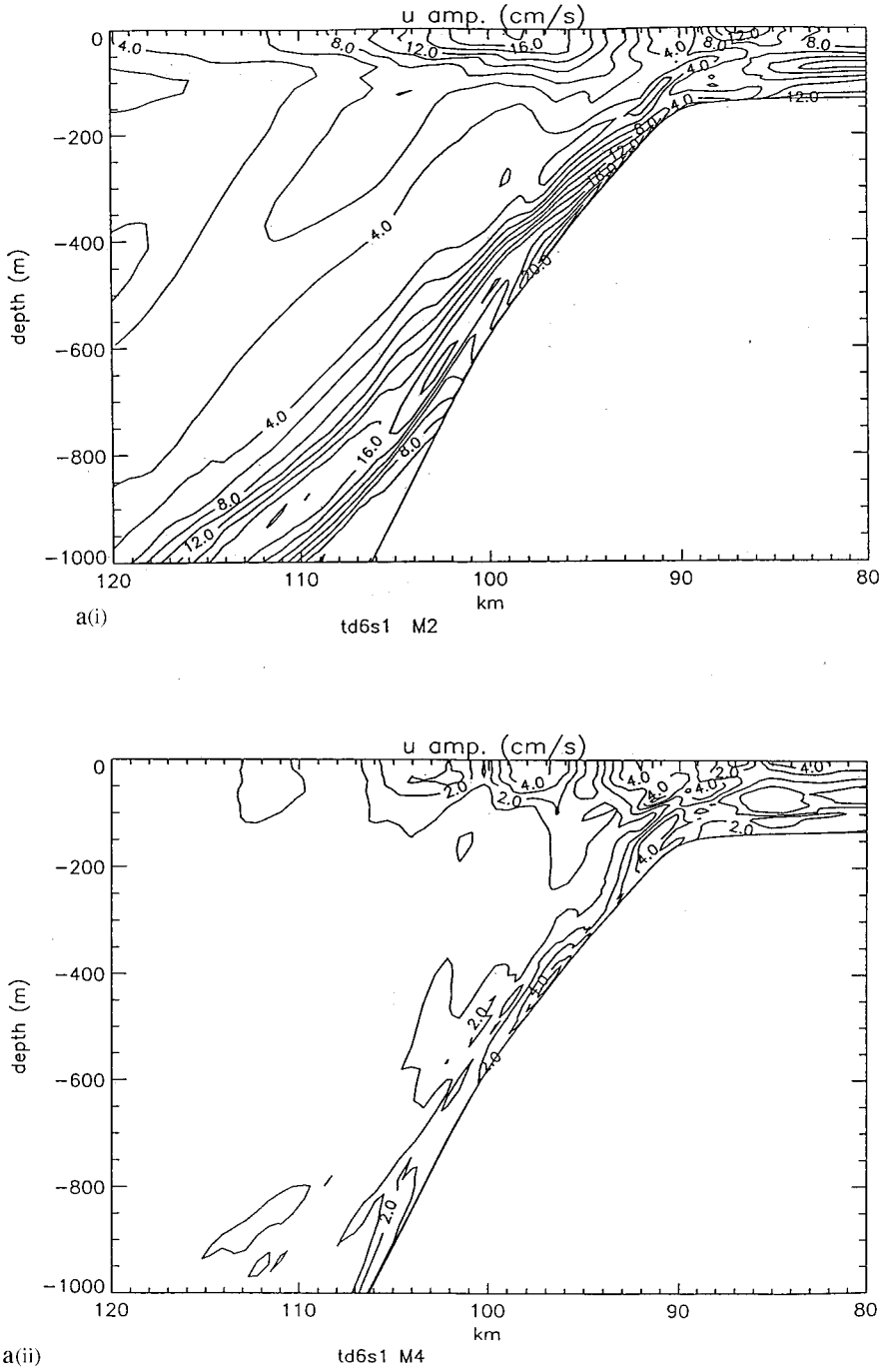

Figure 3. (a) Contours of the amplitude of the u component of the internal tidal current (cm s^{-1}) at (i) M_2 frequency, (ii) M_4 frequency, in the region of the shelf break, computed with the $q^2 - q^2\ell$ turbulence model (Calculation 1). (b) As (a) but for the internal displacement (m) of the density field. (c) Contours of the time averaged over an M_2 period of (i) $\log_{10}$ of the vertical eddy viscosity (m^2 s^{-1}) and (ii) $\log_{10}$ of the turbulence energy (m^2 s^{-2}) in the shelf break region computed with the $q^2 - q^2\ell$ turbulence model.

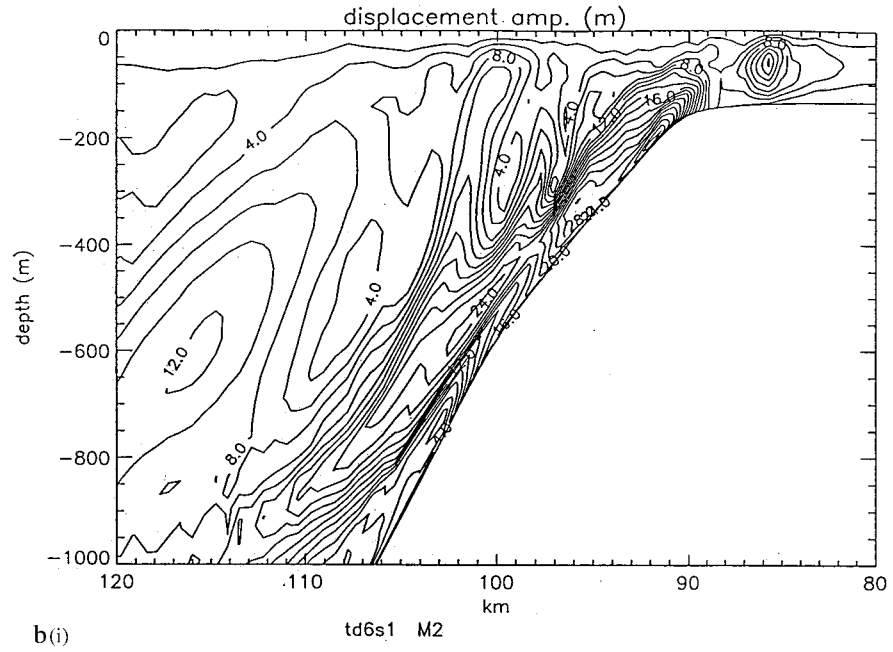

b(i)

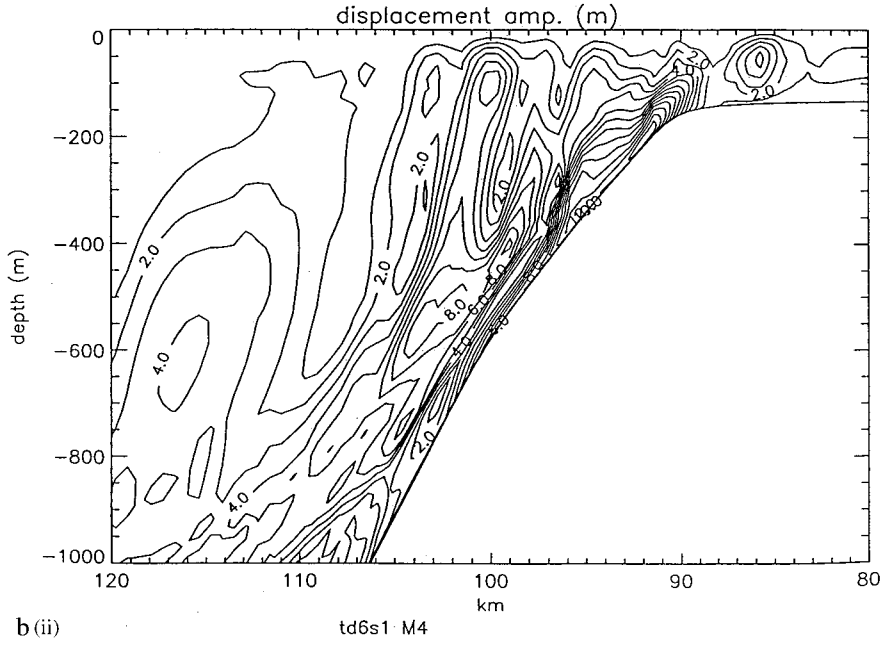

b(ii)

Figure 3 (*Continued*)

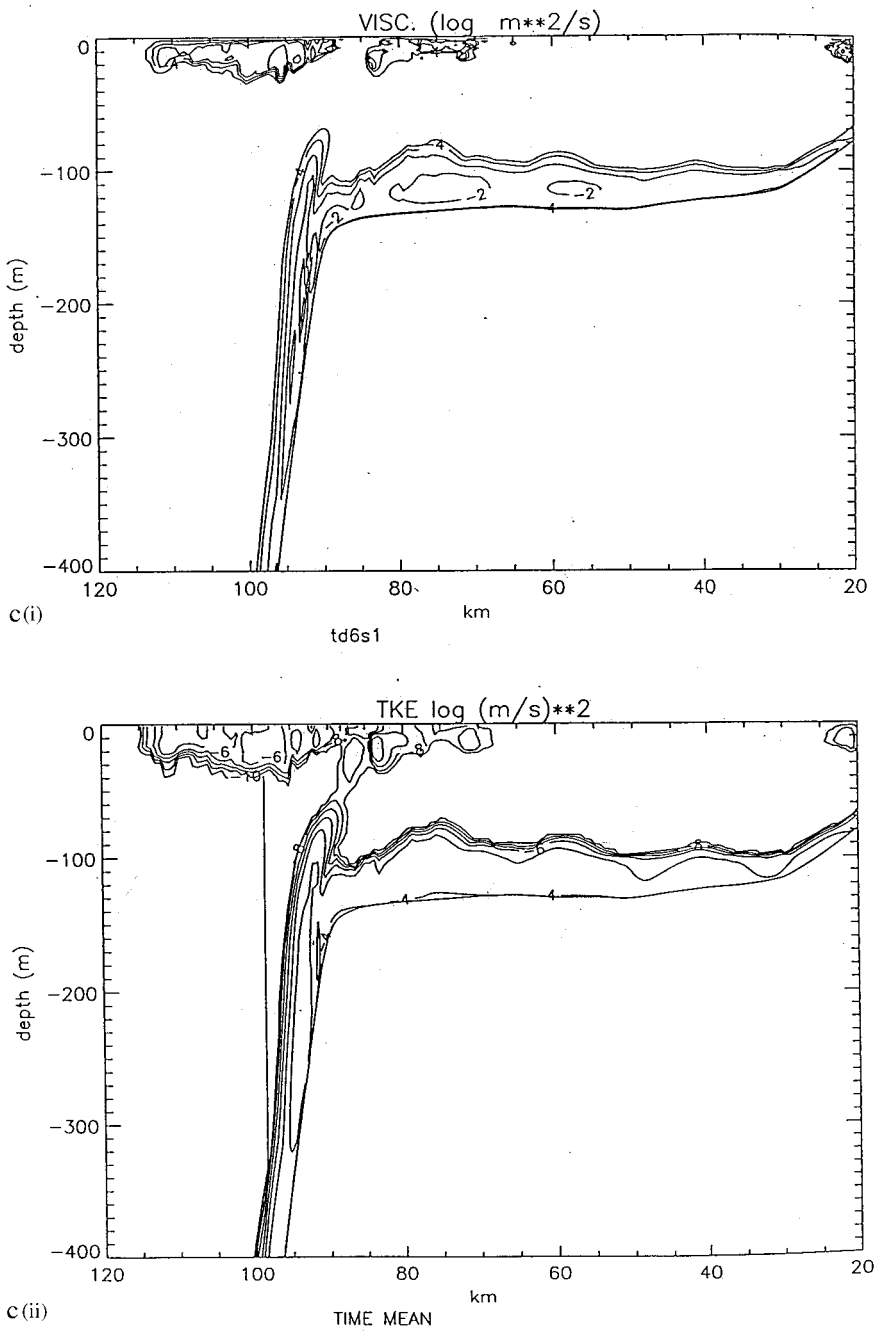

Figure 3 (*Continued*)

Contours of the time averaged over a tidal cycle turbulence energy at the top of the shelf, show (Fig. 3c) a turbulent bottom boundary layer with regions of maximum turbulence corresponding to the locations of maximum amplitude in the near bed tidal currents. The

intensification in the surface and mid-depth tidal currents at the top of the shelf slope (Figure 3(a(i))), gives rise to increased turbulence in this region (Figure 3(c)). This increased mixing in the surface layer at the top of the shelf slope would give rise to an enhanced rate of mixing of surface heating at this location producing a local cooling of the surface water. Observations at a number of shelf break locations [23], exist to support this. Contours of eddy viscosity show similar spatial features to those found for the turbulence energy.

The non-linear terms in the model also generate the higher harmonics of the tide, namely the M_4 and M_6. Contours of the amplitude of the u component of the M_4 tide and its vertical displacement (Figure 3(a(ii),b(ii))) show that the amplitude of the M_4 tide is approximately one fifth of the M_2 tide. The largest M_4 internal displacements and currents occur at approximately the same locations as the strongest M_2 tidal currents and vertical displacements. In these regions the tidal currents are strongest and change most rapidly, hence the non-linear term which is responsible for producing the M_4 tide is a maximum. The M_6 component of the tide (not shown) has a maximum current amplitude in the region of strongest bed current, where the bottom frictional effect is largest. A detailed discussion of the processes producing the higher harmonics of the internal tide is given in Reference [14] and will not be repeated here.

4.3. The k–ℓ model

4.3.1. Identical diffusion coefficients for momentum and density. In a second calculation (Calculation 2, Table 1) the one prognostic turbulence energy submodel was used to predict the turbulence energy (Equation (14)) with eddy viscosity and diffusivity computed from Equation (16), with ℓ_μ and ℓ_λ the mixing lengths for viscosity and diffusivity given by Equation (17). The mixing length ℓ_0 in Equation (17) was computed from the formulation of Xing and Davies [4–6], which, with $\beta = -2$, had been very successful in determining the barotropic tidal current profile in homogeneous shallow seas. In this initial calculation we take $\psi_\mu = \psi_\lambda = 1$, in essence ignoring the effect of stratification on the mixing length, and using the same coefficient for momentum and density mixing, an assumption made by a number of authors [26]. The effect of stable stratification upon turbulence energy is still included through the buoyancy suppression of turbulence in Equation (14).

Contours of the amplitude of the u component of the internal M_2 tide (Figure 4(a)) in the shelf break region show similar features to those found with the two-equation ($q^2 - q^2\ell$) model (Figure 3(a(i))), although the region of strong (of order 20 cm s^{-1}) near bed slope currents found on the shelf slope at 400 m depth is reduced, with near bed current amplitude reduced to the order of 14 cm s^{-1} (Figure 4(a)). Similarly, the extent and magnitude of the near surface region of intensified M_2 currents which occurs at approximately 95 km offshore is reduced in the k–ℓ model. A comparison of internal displacements (Figure 4(b) with Figure 3(b(i))) also shows that although the same major features are present the intensity of the internal displacement has been reduced with the k–ℓ model.

Contours of the time mean turbulence energy and eddy viscosity (Figure 4(c)) computed with the k–ℓ model show similar features to those derived previously using the $q^2 - q^2\ell$ model. In particular, the turbulence energy intensity shows a turbulent bottom boundary layer, with turbulence intensity varying over the shelf with a space scale consistent with that found using the $q^2 - q^2\ell$ model (compare Figure 4(c) with Figure 3(c)). The viscous bottom boundary layer, however, has a larger extent than that found previously. The reason for this is that in the $q^2 - q^2\ell$ model the computed mixing length, although exhibiting a similar parabolic variation through depth to that computed using Equation (18) [5,6], is reduced in magnitude in regions of stable stratification such as those that occur here at about 75 m depth.

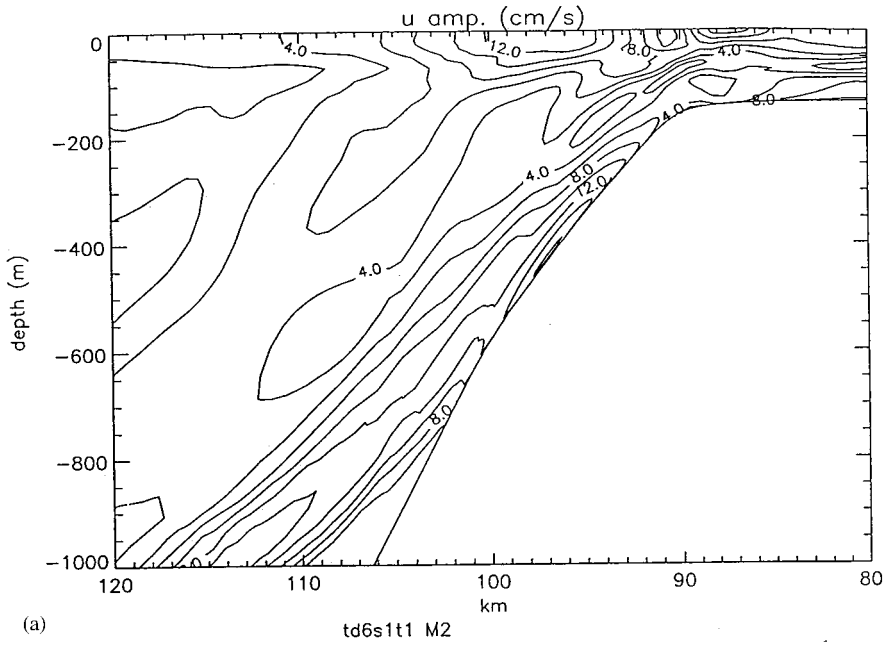

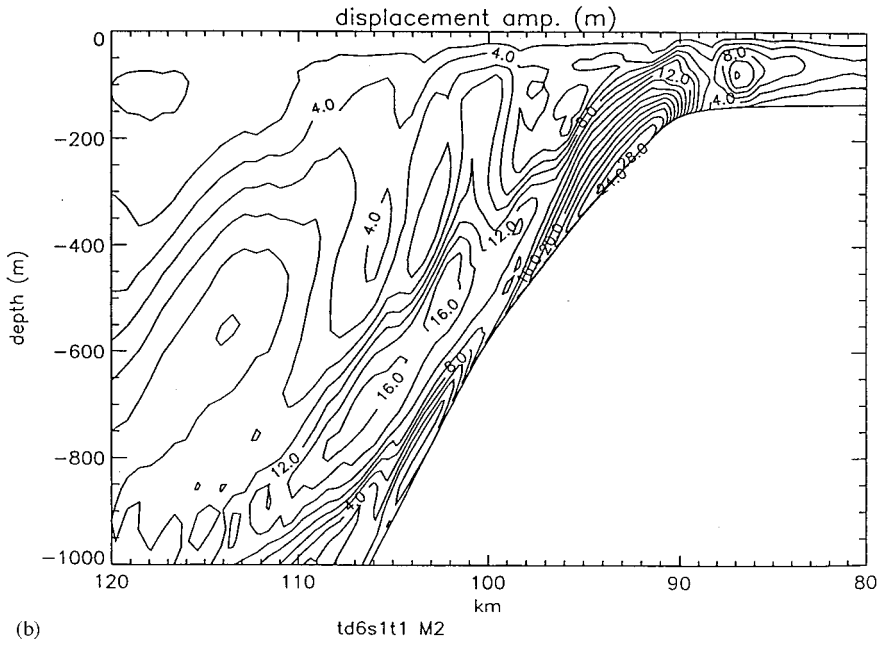

Figure 4. (a) Contours of the amplitude of the u component of the M_2 internal tidal current (cm s^{-1}) computed with the k–ℓ model with $\psi_\mu = \psi_\lambda = 1$ (Calculation 2). (b) As (a) but for the internal displacement (m) of the density field. (c) Contours of the time average of $\log_{10}$ of the vertical eddy viscosity (m^2 s^{-1}) and (d) $\log_{10}$ of the turbulence energy (m^2 s^{-2}) calculated with the k–ℓ model (Calculation 2).

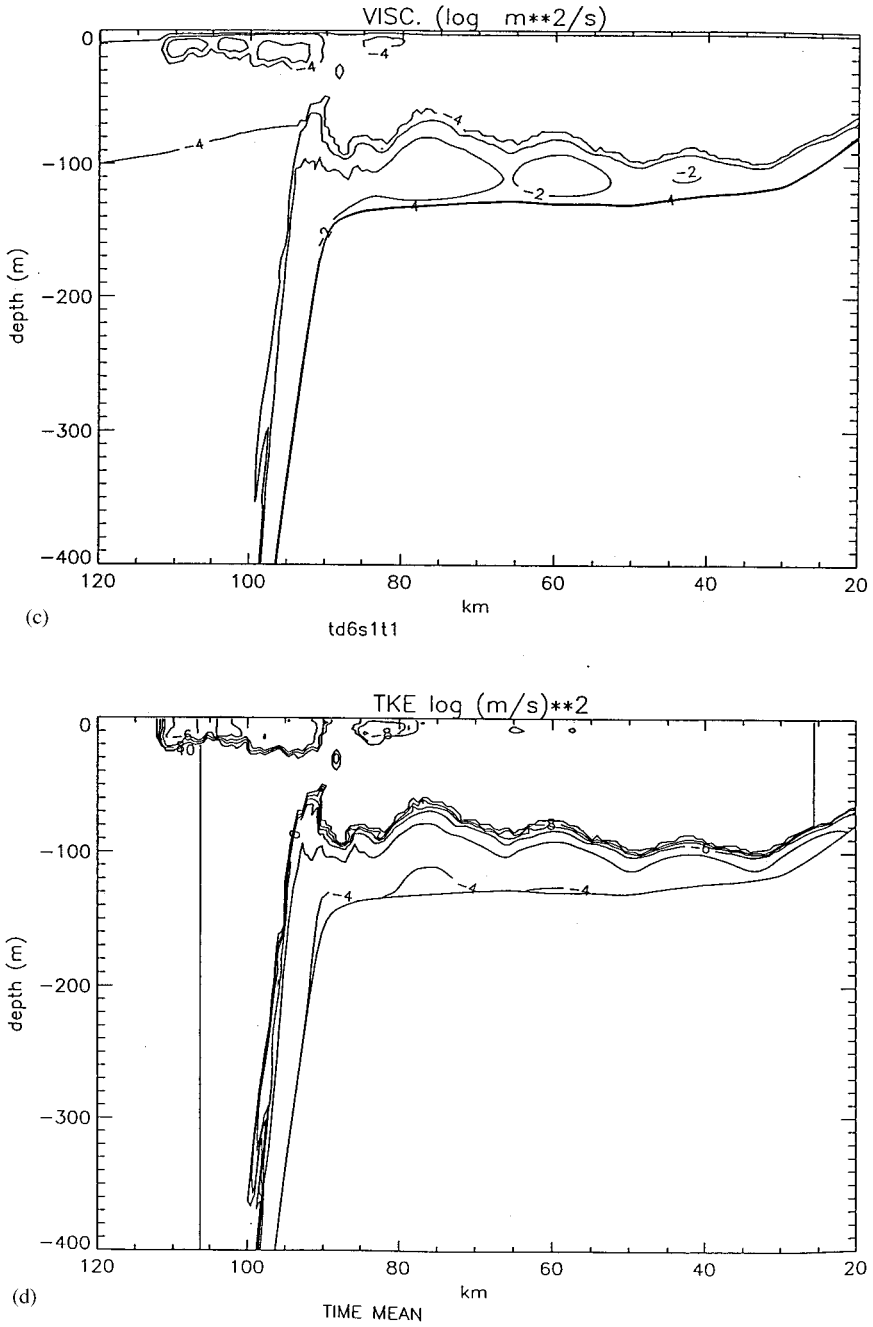

Figure 4 (*Continued*)

Consequently the mixing length and hence the computed eddy viscosity and diffusivity which are its product with the turbulence energy are reduced in the $q^2 - q^2\ell$ model but not in the k–ℓ model. In the k–ℓ model the eddy diffusivity is the same as the eddy viscosity, therefore, this will produce more mixing at the level of the thermocline and reduce the internal tide.

4.3.2. Application of mixing length stability functions. In a subsequent calculation (Calculation 3) the single prognostic turbulence energy equation was again used, with ℓ_0 computed as before, but using Equation (13) to compute A_v and K_v, which were different due to differences in S_M and S_H. Contours of the amplitude of the u component of the internal tidal current in

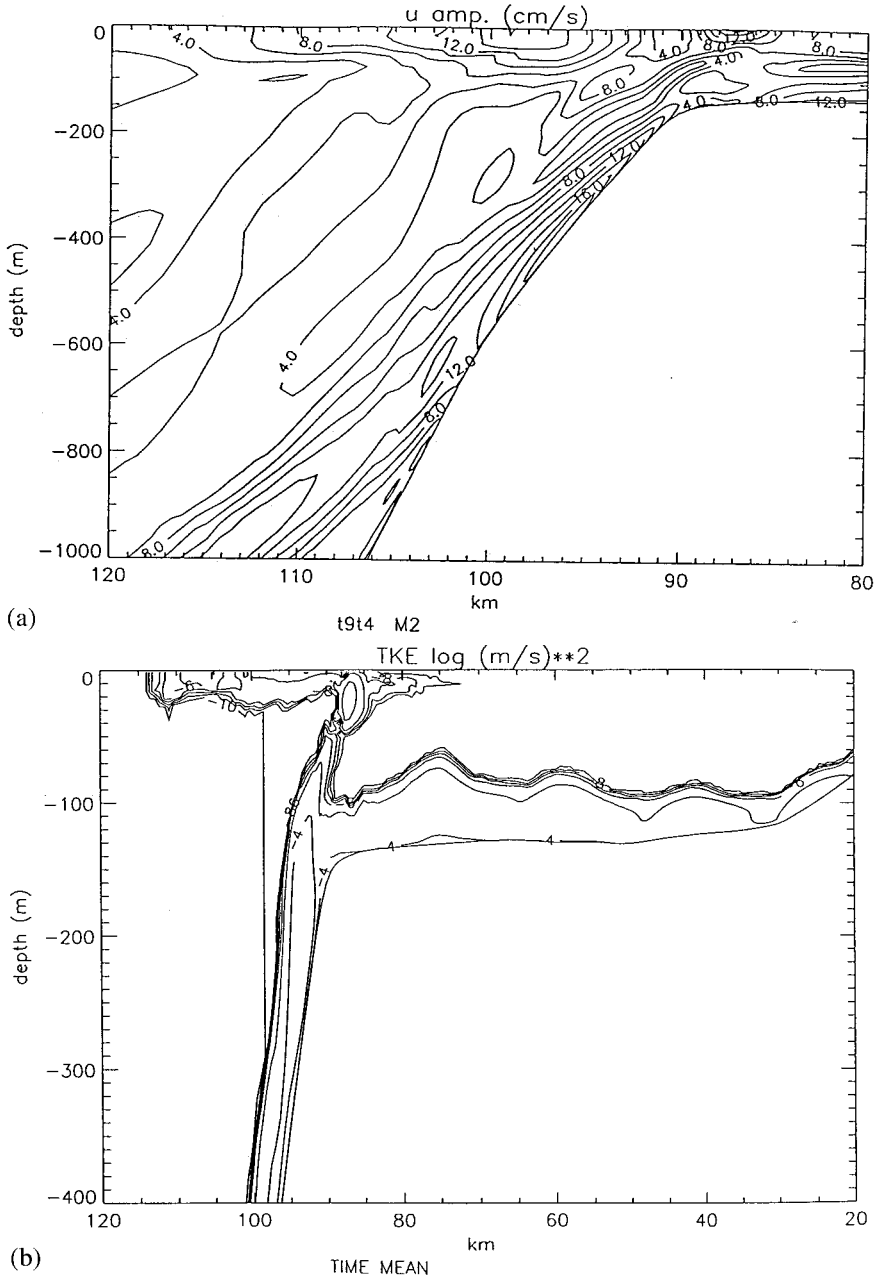

Figure 5. (a) Contours of the amplitude of the u component of the M_2 internal tidal current (cm s^{-1}) computed with the k–ℓ model and stability functions S_H and S_M (Calculation 3). (b) Contours of the time average of $\log_{10}$ of the turbulence energy (m^2 s^{-2}) calculated with the k–ℓ model and stability functions S_H and S_M (Calculation 3).

the region of the shelf break (Figure 5(a)) show a near surface region approximately 95 km offshore, where the u current amplitude is of the order of 14 cm s^{-1}. A region of strong (of order 18 cm s^{-1}) near bed currents are found on the shelf slope at a depth of approximately 400 m. These features are similar (although with a slight reduction in current amplitude and a slightly increased thickness of the bottom boundary layer) to those found with the $q^2-q^2\ell$ model. Obviously, the effect of reducing the diffusion coefficient for density decreases the mixing, and the currents computed with the k–ℓ model are in closer agreement with those determined using the $q^2-q^2\ell$ model. Contours of the internal displacement, (not shown) have a region of very rapid increase in internal displacement at the top of the shelf slope in close agreement with that found for the $q^2-q^2\ell$ model.

Contours of turbulence energy, eddy viscosity and diffusivity computed with this k–ℓ model are similar to those determined with the $q^2-q^2\ell$ model (compare Figure 5(b) with Figure 3(c)).

4.3.3. The JX mixing length modified by a stability function. In the previous calculation (Calculation 3) the mixing length was not reduced by the influence of stable stratification, although this effect is present in the $q^2-q^2\ell$ model. To examine this the JX mixing length ℓ_0, as computed previously, was modified using the Richardson number dependent stability function ψ (Equation (25)) and this modified mixing length was used in Equation (13) to determine A_v and K_v (Calculation 4). Contours of u current amplitude and internal displacement (Figure 6(a) and (b)) at the M_2 period computed with this form of the mixing length exhibit the main features found previously using both the $q^2-q^2\ell$ and JX mixing length, with some slight intensification at the top of the shelf slope (compare Figure 3(a(i)), 3(b(i)) and 6(a) and (b)).

Contours of turbulence energy and viscosity (with diffusivity the same as viscosity) show similar spatial distributions to those found previously with some slight changes in the region of the slope.

4.3.4. The JX mixing length modified by ψ_μ and ψ_λ. In a final calculation using the JX mixing length formulation (Calculation 5), the mixing lengths ℓ_μ and ℓ_λ were determined, also using Equation 17, with ψ_μ and ψ_λ given by Equation (23) and ℓ_μ and ℓ_λ were then used in Equation (16). Contours of the amplitude of the u component of velocity and internal displacement (not shown) for the M_2 tide (Figure 7(a)), derived with these mixing length formulations show the same general features as those found previously, with some small modifications in the near bed region of the shelf slope. Contours of turbulence energy (Figure 7(b)) and viscosity (not shown), although exhibiting similar spatial distributions to those found previously, show a slightly thinner turbulence bottom boundary layer than that occurring in previous calculations. This is due to the reductions in viscosity and diffusivity produced by the stability functions ψ_μ and ψ_λ, although the viscosity and diffusivity are still larger than those found with the $q^2-q^2\ell$ model

4.4. Richardson number model

An alternative to using turbulence energy submodels to compute mixing coefficients, is to determine them from simple expressions (Equation (21)) in terms of a local Richardson number (Calculation 6, Table 1). Values of the local Richardson number were not allowed to exceed 20, which effectively gave a background viscosity corresponding to the A_0 and B_0 values given in Equation (21). Contours of the amplitude of the u component of the M_2 internal tidal current in the region of the shelf break (Figure 8(a)), show strong near bed currents (of order

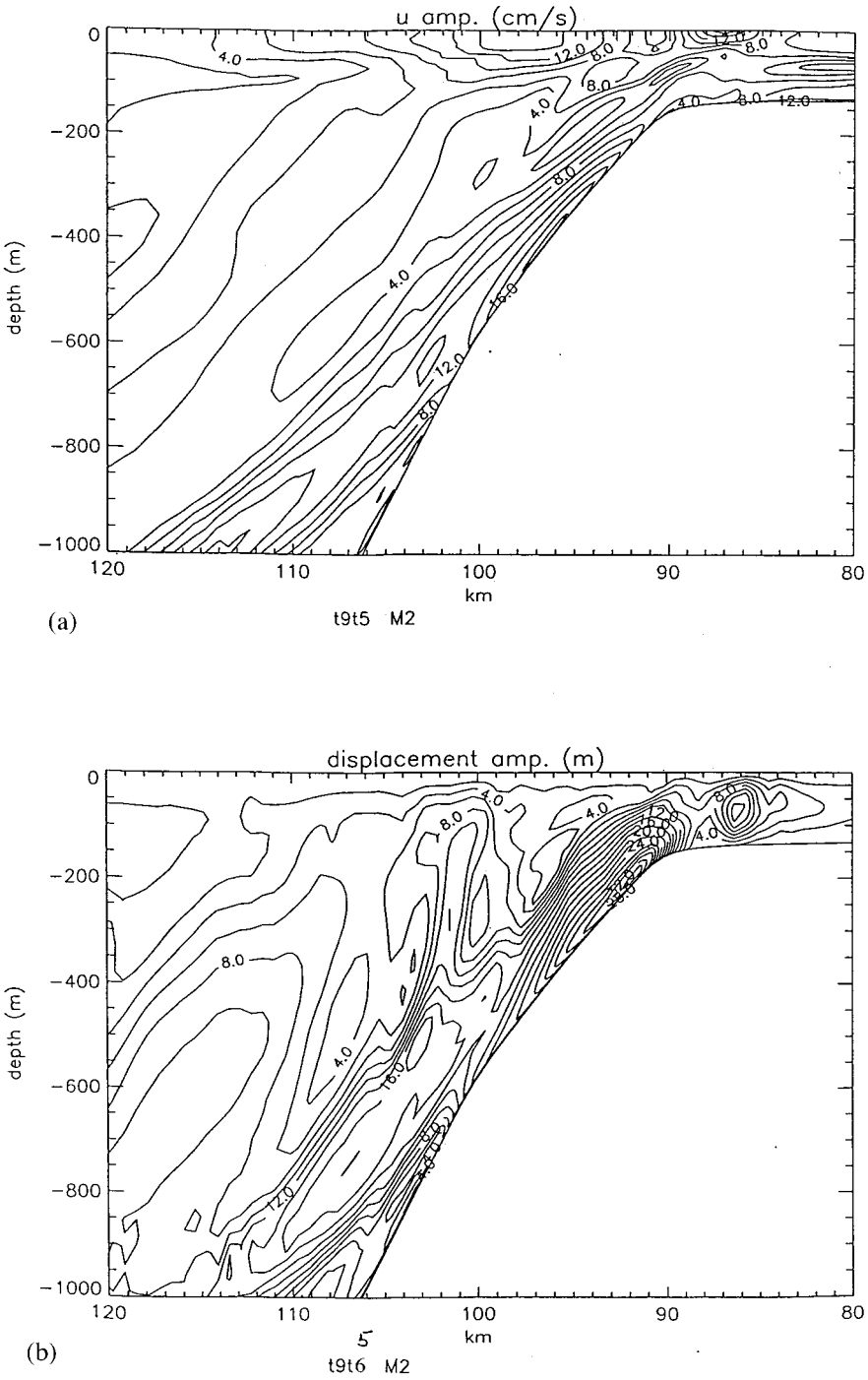

Figure 6. (a) Contours of the amplitude of the u component of the M_2 internal tidal current (cm s^{-1}) computed with the k–ℓ model with $\ell = \ell_0 f(R_i)$ (Calculation 4). (b) As for (a), but for the internal displacement (m) of the density field.

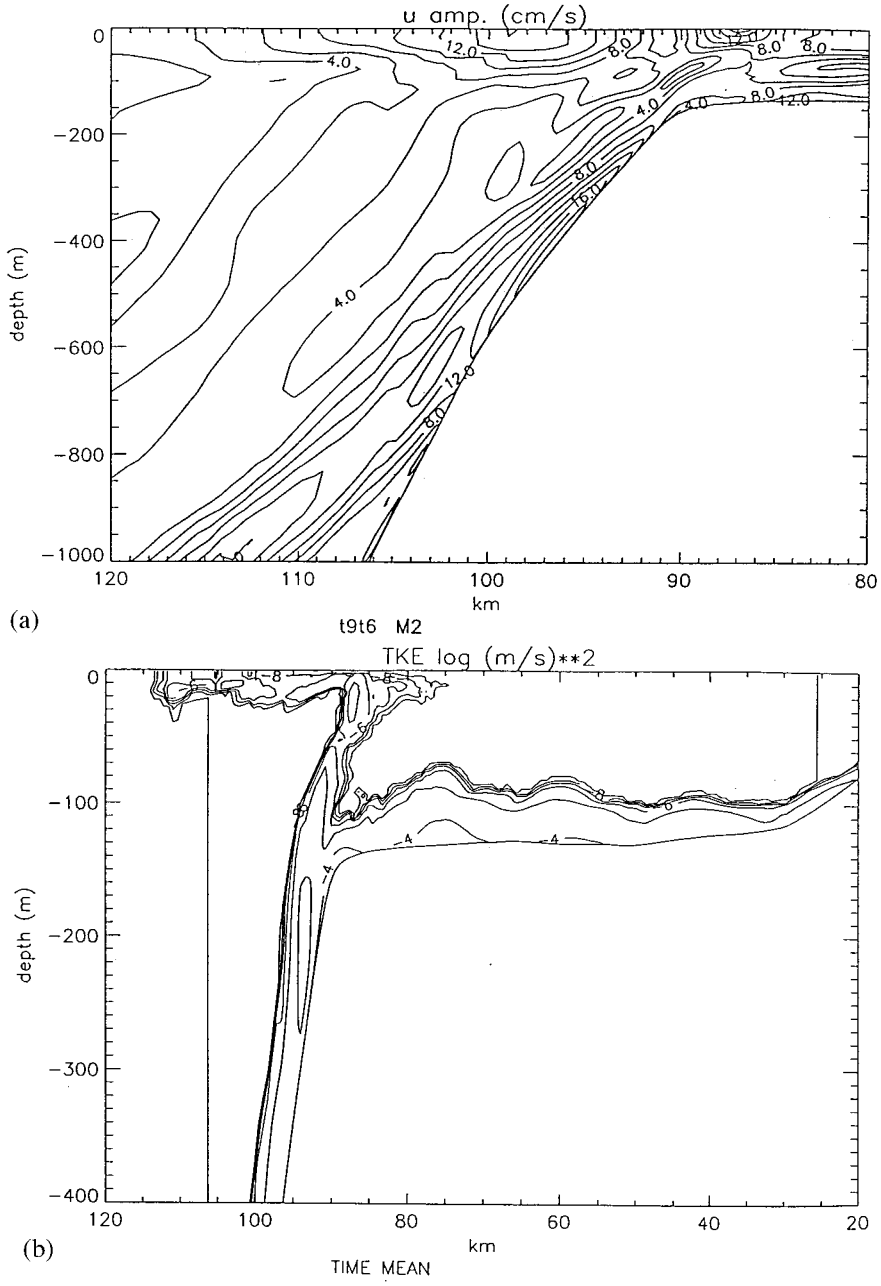

Figure 7. (a) Contours of the amplitude of the u component of the M_2 internal tidal current (cm s^{-1}) computed with the k–ℓ model with stability functions ψ_μ and ψ_λ (Calculation 5). (b) Contours of the time averaged of $\log_{10}$ of the turbulence energy (m^2 s^{-2}) calculated with the k–ℓ model with stability functions ℓ_μ and ℓ_λ (Calculation 5).

20 cm s^{-1}) on the shelf slope at a depth of 400 m, with a region of strong (of order 16 cm s^{-1}) near surface currents located approximately 95 km offshore. The intensity and spatial distribution of the u current amplitude (Figure 8(a)) and internal displacement (Figure 8(b)),

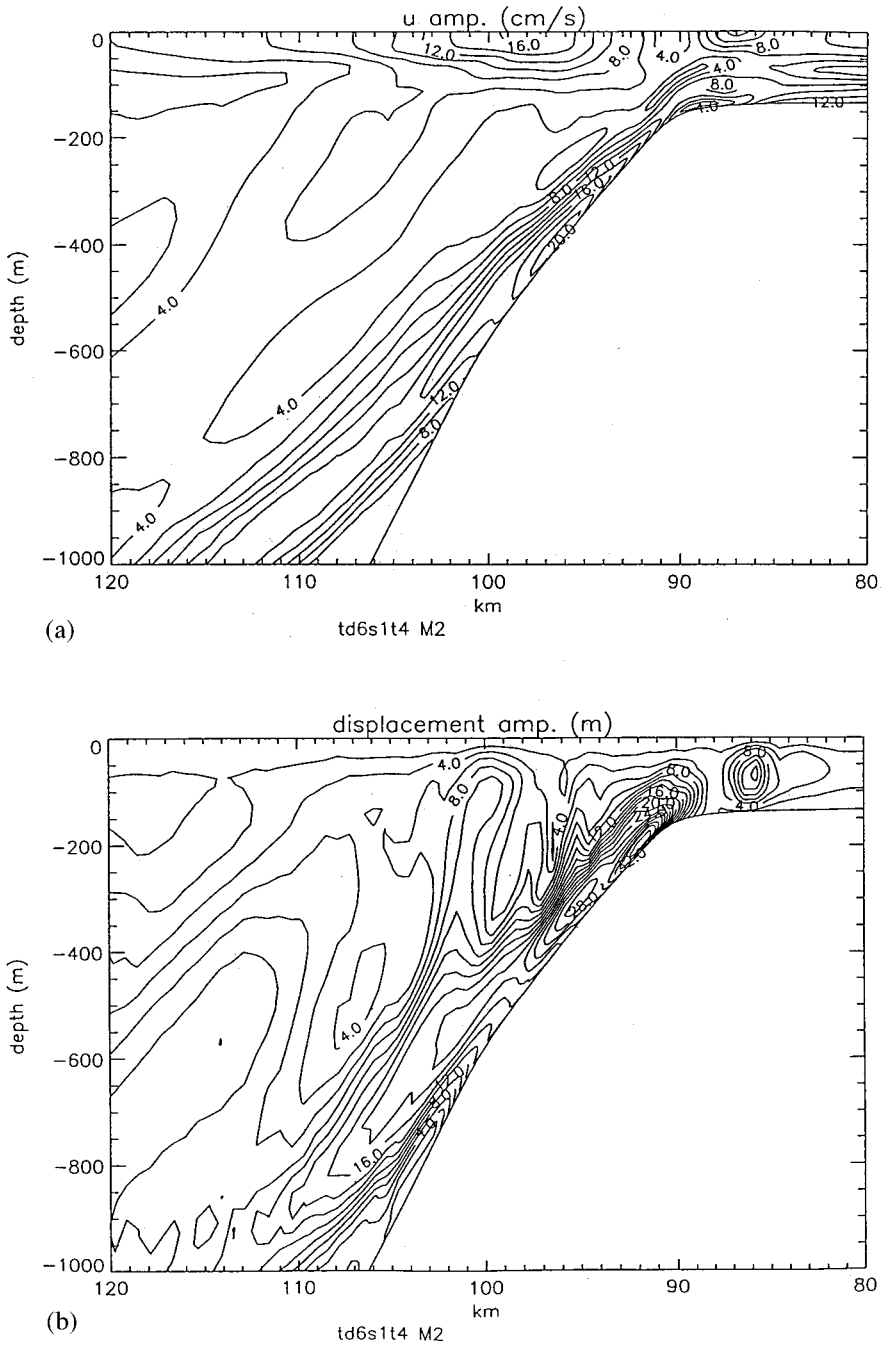

Figure 8. (a) Contours of the amplitude of the u component of the M_2 internal tidal current (cm s^{-1}) computed using a Richardson number dependent viscosity (Calculation 6). (b) As (a) but for the internal displacement (m) of the density field.

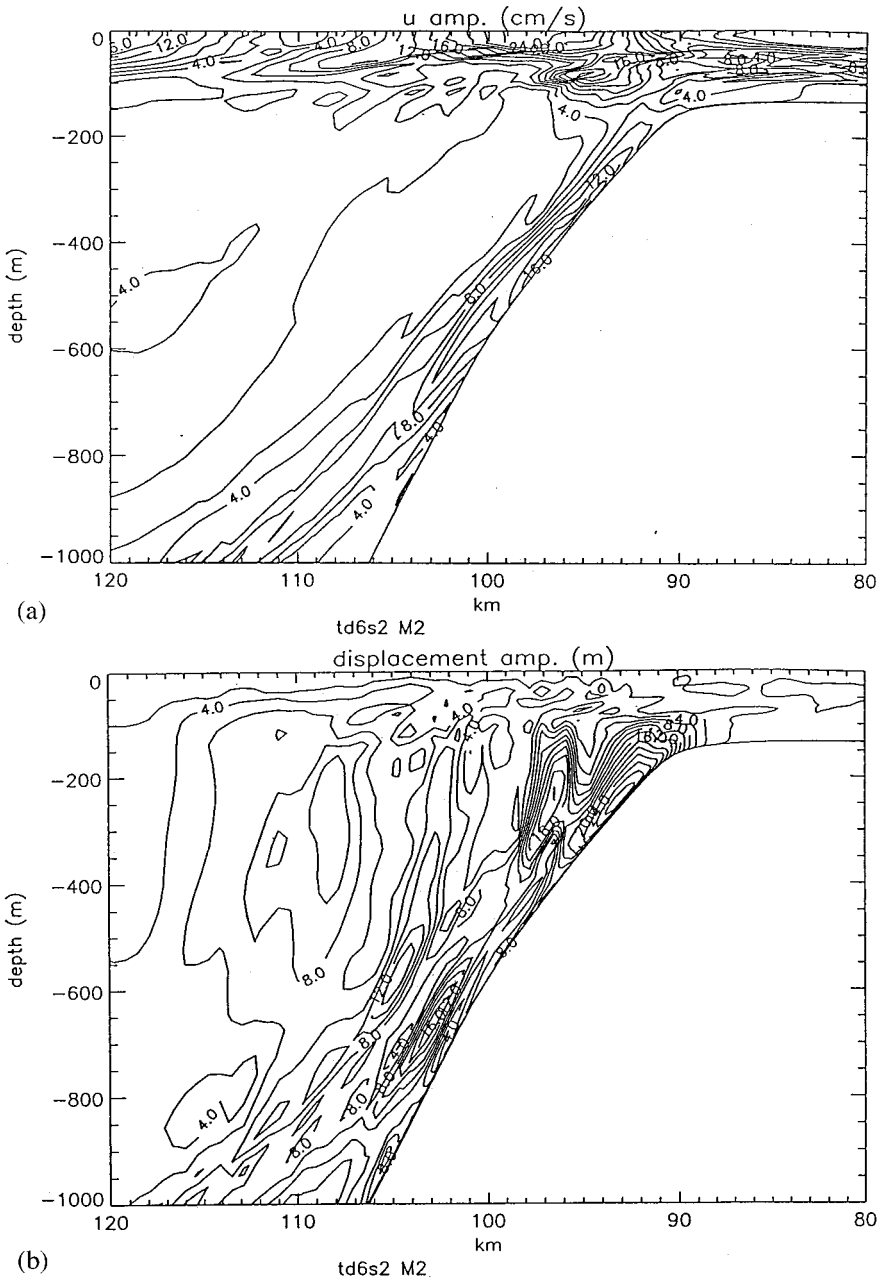

Figure 9. (a) Contours of the amplitude of the u component of the internal tidal current (cm s^{-1}) at the M_2 frequency in the region of the shelf break, with typical summer stratification computed with the $q^2 - q^2\ell$ model (Calculation 7). (b) As (a) but for the internal displacement (m) of the density field. (c) Contours of the time averaged of $\log_{10}$ of the turbulence energy, (m^2 s^{-2}) calculated with the $q^2 - q^2\ell$ model and typical summer stratification (Calculation 7).

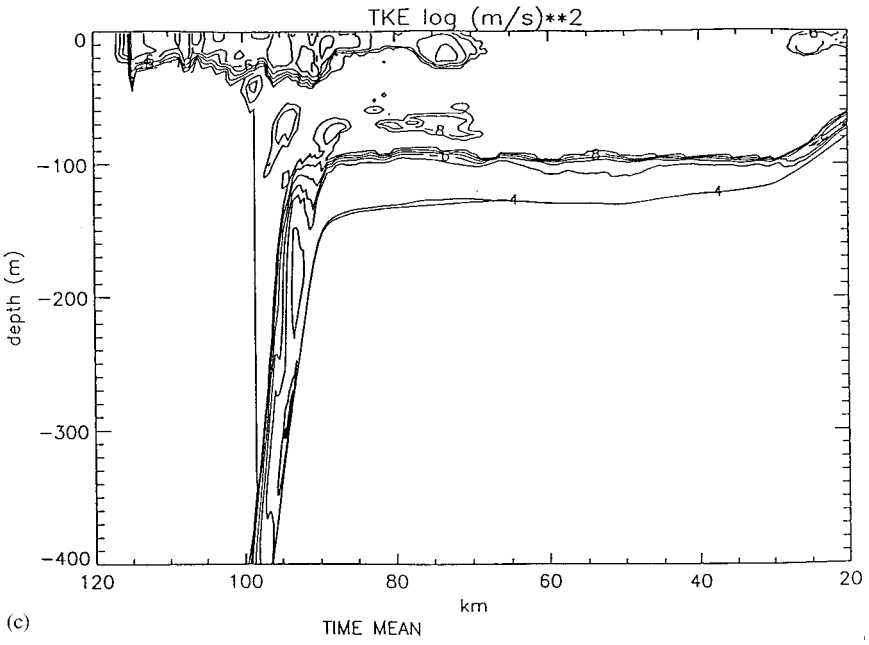

Figure 9 (*Continued*)

computed with a simple Richardson number dependent eddy viscosity is very close to that found previously with the $q^2 - q^2\ell$ model (Figure 3(a) and (b)). This suggests that the major features of the internal tide, namely current amplitude and internal displacement, can be reproduced by these simpler models provided they do not produce excessively large vertical diffusion coefficients.

5. SENSITIVITY OF THE INTERNAL TIDE TO DENSITY CHANGES

5.1. Summer stratification

In the previous series of calculations using a range of turbulence energy submodels, a temperature profile which is characteristic of a winter period was considered. Here we will examine the influence of summer stratification (Figure 2) upon the internal tide (Table 1, Calculation 7). For consistency with the detailed winter calculation, the $q^2 - q^2\ell$ turbulence model is used with the idealized initial temperature profile given in Figure 2, derived from summer observations [25]. As in the previous series of calculations, the model was integrated forward in time for 30 tidal cycles before comparisons are made with previous calculations.

Comparing the summer and winter profiles (Figure 2) it is evident that in the summer the surface temperature is significantly higher (14°C compared with 10°C) with temperature decreasing to 8°C over a water depth of the order of 100 m. (In winter the surface layer is only of the order of 70 m). Below the surface 100 m layer the two temperature profiles are identical. The stronger surface temperature gradient in summer gives rise to a significantly larger value of N^2. A comparison (namely summer/winter) of contours of the amplitude of the u component of the M_2 internal tidal current (Figure 9(a(i)) and Figure 3(a(i))), shows that near the top of the shelf edge the maximum amplitude of the near bottom u component of current

in summer is slightly less than in winter (16 cm s^{-1} compared with 20 cm s^{-1}). However, the maximum surface amplitude of 24 cm s^{-1} in summer is significantly larger than the 16 cm s^{-1} found in winter. Also, the surface amplitude of the u component of current both on the shelf and as far offshore as 120 km is significantly larger in summer than in winter (compare Figure 9(a) with Figure 3(a(i))). The internal displacement amplitude at the M_2 tidal frequency in the summer (Figure 9(b)) shows a region of strong internal displacement near the top of the shelf break, with a second region of maximum displacement in the near bed region at about 105 km from the shore. This distribution is similar to that found for the winter period (Figure 3(b(i))), although in the summer, unlike the winter, there is no significant displacement on the shelf.

The amplitude of the u component of the M_4 tide in summer (not shown) exhibits a comparable near bed intensification at about 95 km (water depth 400 m) offshore to that found in winter (Figure 3(a(ii))). This similarity is to be expected because at this depth the two density profiles (summer and winter) are identical. The current amplitude in the near surface layer in summer is significantly stronger than in winter due to the differences in density. Contours of the internal displacement in the summer (not given) reveal that the maximum displacement, as in the winter, is located along the shelf edge, although in the summer there is no significant internal displacement on the shelf, which is very different to that found in the winter (Figure 3(b(ii))). As in the winter calculation, the region of strongest M_4 production is above the shelf break where the non-linear terms are at a maximum.

Contours of the amplitude of the u component of current, and the internal displacement at the M_6 period (not shown) show that in summer the current amplitude is larger than in winter and is again confined to the surface layers above the upper part of the shelf slope and on the shelf. Internal displacement contours also show a maximum (significantly larger than in winter) in the region of the upper part of the shelf slope. The location of these maxima in the M_6 internal tide coincide with the positions where the density surfaces show maximum distortion (i.e. steepening of the leading edge of the wave propagating along a density surface) as the internal tide propagates on and off the shelf. (A detailed discussion of this is given in Reference [14] and will not be repeated here).

Turbulence energy contours (Figure 9(c)) show similar characteristics to those found in the winter (Figure 3(c)), with turbulence energy being a maximum in the near bed region along the shelf slope and on the shelf (Figure 9(c)), and with turbulence decreasing with height above the bed. The horizontal spatial variability of the near bed turbulence and viscosity (not shown) is significantly more uniform in the summer than in the winter. The reason for this is that in the winter there appears to be a strong mode two internal tide on the shelf (Figure 3(a) and (b) with associated regions of more intense mixing. In the summer this feature does not occur and the turbulent bottom boundary layer is more spatially uniform. The region of enhanced surface mixing is comparable with that found in the winter, although the two regions do not overlap. (The overlap between the surface and bed turbulence layers at the shelf break found in winter appears to be associated with the thicker bed turbulence layer at the sea bed which occurs in winter, rather than the surface layer).

This comparison between summer and winter conditions clearly shows that seasonal variations in the density field make significant differences to the amplitude of the internal tidal current and the associated displacement. These differences are significantly larger than those found for the winter situation using different turbulence energy models, and suggest that although slight differences in the solution will arise if different turbulence submodels are used, the main differences between summer and winter will be correctly reproduced by the different models.

However the changes in temperature profile and hence N^2 between winter and summer are quite significant. The next section discusses whether small changes in stratification, comparable with the errors in trying to determine an initial synoptic temperature field from a limited set of observations, are comparable with the differences found with the different turbulence submodels. This is particularly important because if the differences produced by small perturbations of the density field are comparable with those due to the use of different turbulence models, this suggests that it may be difficult to determine from measurements which submodel is correctly reproducing the internal mixing produced by the internal tide. In an initial series of calculations a small perturbation to the initial density field corresponding to a winter situation is considered.

5.2. Sensitivity of the internal tide to small density perturbations

5.2.1. Winter period. In this section we initially consider the sensitivity of the internal tide in winter to a small perturbation of the winter density field (Calculation 8, Table 1) with a subsequently similar perturbation to the summer situation (Calculation 9, Table 1). In both cases we solve the fully non-linear system of equations with diffusion determined from the $q^2 - q^2\ell$ turbulence closure model.

The temperature profile used in the calculation (Figure 10), corresponds to a slight decrease in temperature at depth, and a small change in the near surface layer, (compare Figure 10 with Figure 2), producing a variation in the profile of N^2.

Although they show features similar to those found previously (Figure 3(a)), namely a region of strong (amplitude 20 cm s^{-1}) bottom currents on the shelf slope at about 400 m, contours of the amplitude of the u component of the M_2 tide (Figure 11(a)) exhibit different features in the surface layer. In particular, the region of strong surface currents that occurs at 100 km offshore (Figure 3(a)) is no longer present (Figure 11(a)), although the surface currents on the shelf have been intensified. Also, the region of strong currents (amplitude of order up to 16 cm s^{-1}) found at 115 km offshore and a depth of 1000 m, are no longer present.

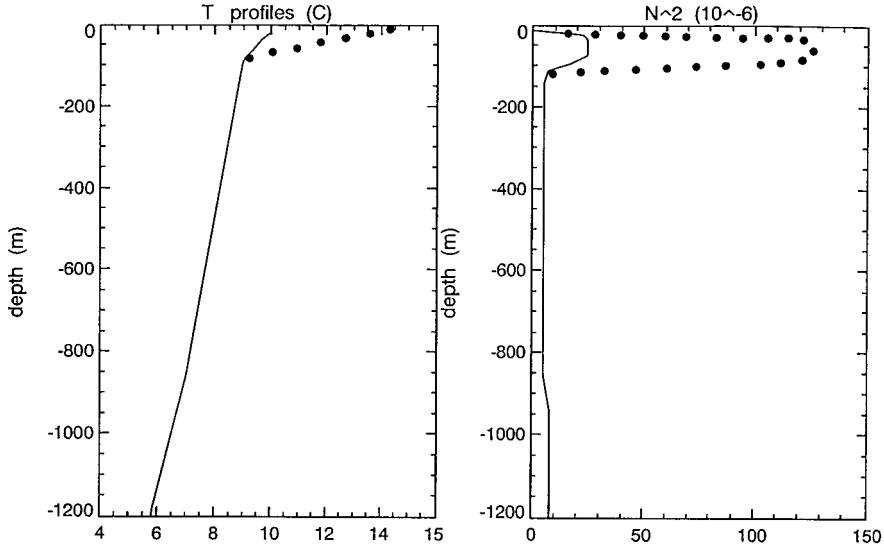

Figure 10. Profiles of the temperature T(°C) and Brunt–Vaisala frequency $N^2 \times 10^{-6}$ (s^{-2}) for a perturbed winter (solid) and perturbed summer (dotted) stratification.

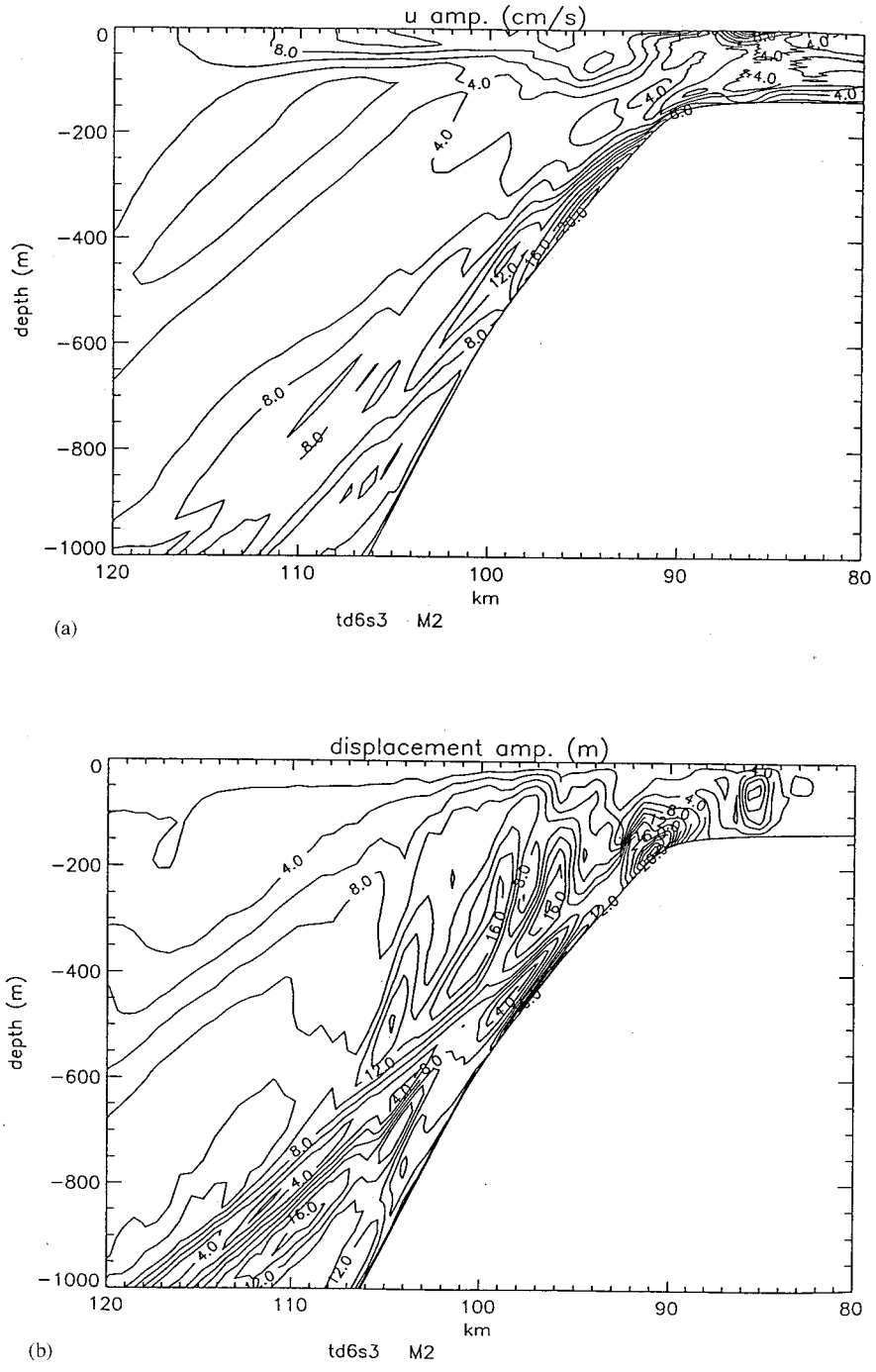

Figure 11. (a) Contours of the amplitude of the u component of the internal tidal current (cm s^{-1}) computed using the $q^2 - q^2\ell$ model with the perturbed winter density field (Calculation 8). (b) As (a) but for the internal displacement (m) of the density field.

Comparing the amplitude of the M_2 internal tidal displacement (Figure 11(b)) with that found previously (Figure 3(b)), it is evident that although in both calculations there is a region at the top of the shelf break where the internal tidal displacement is large, with a similar region having a mid-water maximum on the shelf, the exact shape and extent of these regions is different. Also, the magnitude and spatial distribution of the internal displacement in offshore regions (between 110 and 120 km) is significantly different.

5.2.2. Summer period. The temperature profile used in this calculation (Calculation 9, Table 1), corresponds to a reduction in temperature below the surface layer (compare Figure 10, with Figure 2), producing a change in the Brunt–Vaisaila frequency (N^2), at depth.

Contours of the amplitude of the M_2 tidal current (Figure 12(a)), although showing similar features to those occurring previously (Figure 9(a)), namely regions of strong near surface current, show much weaker bottom currents along the shelf slope due to the change in density in this area. Contours of the internal displacement amplitude at the M_2 period (Figure 12(b)), show a region of large displacement (exceeding 16 m) at the top of the shelf break with a region of mid-water internal displacement on the shelf. The region of significant internal displacement at 700 m depth found previously (Figure 9(b)) is no longer present due to the change in density. This spatial distribution of internal displacements is significantly different to that found previously (Figure 9(b)), in particular the absence of the internal displacement at 700 m. A comparison of Figure 12(b) with Figure 9(b) shows that offshore (between 110 and 120 km) the amplitude of the internal displacement calculated with the new summer stratification is larger than those found previously.

Comparing the amplitude of the u component of current at the M_4 tidal frequency, (not shown) with that obtained previously showed that the spatial variability in the near surface layer was similar, although the current magnitude had been reduced and the area of intensified M_4 tidal currents which occurred previously on the shelf slope had been reduced. A similar picture emerged from a comparison of the internal displacements (not shown) which showed that the area where internal displacements exceed 6 m, found previously in the shelf slope region at 700 m, did not occur in the present calculation due to the modification of the density field at this depth. Also the M_4 internal displacement near the top of the shelf slope had been reduced, suggesting that this change in stratification and the associated reduction in the internal tide had reduced the non-linear mechanisms, giving rise to the higher harmonics. This was confirmed by comparing the internal displacement of the M_6 internal tide (not shown) with that found previously. From this comparison it is evident that the region of large (amplitudes exceeding 6 m) M_6 internal displacement that occurred previously along the shelf slope at a depth of 300 m is no longer present.

Contours of turbulence energy (Figure 12(c)) and eddy viscosity (not presented) show that in the present calculation the near bed region of strong turbulence energy and viscosity is restricted to the area at the top of the shelf break and the near bed region on the shelf, in contrast to the previous calculation in which the region of intensified turbulence energy extended further down the slope (Figure 9(c)). The production of turbulence at depth in the previous calculation and its absence in the present calculation is consistent with the much stronger shelf slope currents at depth found previously, which are responsible for the turbulence generation and the absence of these currents in this case. Enhanced surface turbulence energy and viscosity in the region above the shelf break does not appear to be significantly different from that found previously.

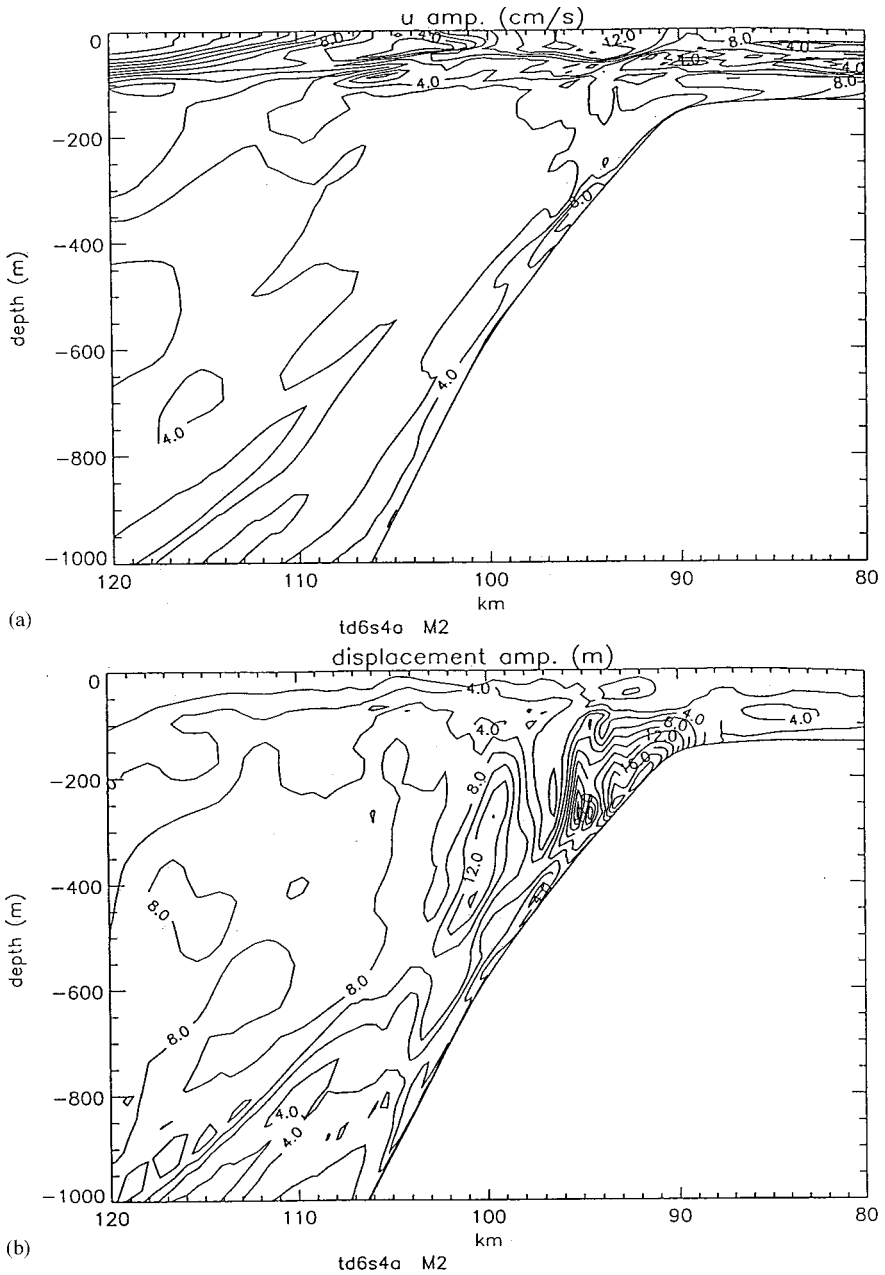

Figure 12. (a) Contours of the amplitude of the u component of the internal tidal current (cm s^{-1}) at the M_2 frequency, using the $q^2 - q^2\ell$ model with the perturbed summer stratification (Calculation 9). (b) As (a) but for the internal displacement (m) of the density field. (c) Contours of the time averaged of $\log_{10}$ of turbulence energy, ($m^2\ s^{-2}$) calculated with the $q^2 - q^2\ell$ model and typical summer stratification (Calculation 9).

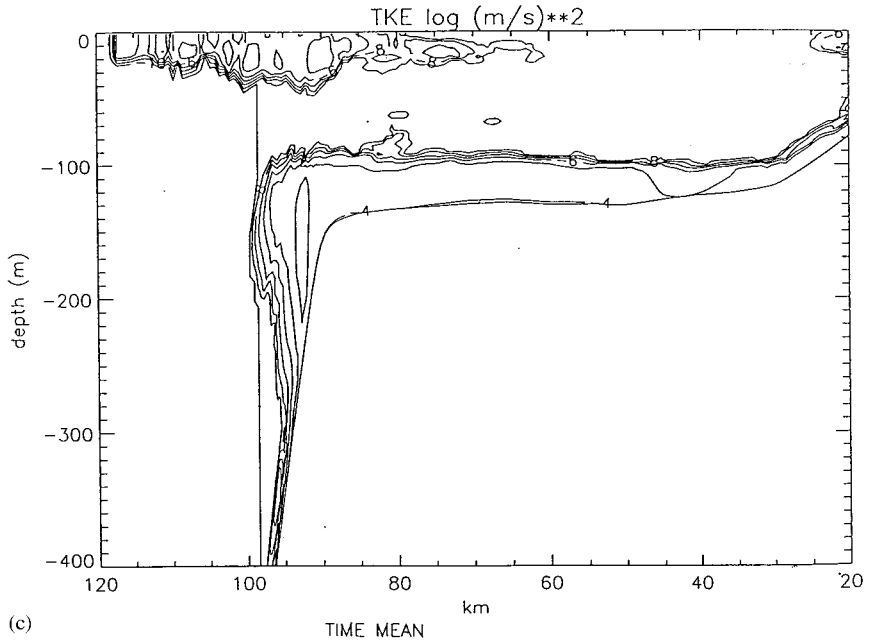

Figure 12 (*Continued*)

6. CONCLUDING REMARKS

In this paper we have outlined the major stages in developing a three-dimensional non-linear hydrodynamic model with a range of submodels for computing the vertical diffusion of momentum and density. Calculations have been performed using the model in cross shelf form to examine the generation of the internal tide in the shelf edge region off the west coast of Scotland under idealized conditions of winter and summer stratification. The model uses a sigma co-ordinate in the vertical with a finite difference grid of 50 sigma levels, and a horizontal grid of order 0.6 km. This resolution was found to be sufficiently accurate to resolve the major features of the internal tide in the area [13] [14]. Calculations using a range of turbulence energy submodels show that the internal tide computed with a prognostic equation for turbulence energy accounting for buoyancy effects and an algebraically specified mixing length [4,12] in which the effects of stratification upon the mixing length were ignored, was slightly different from that computed using the two prognostic equations $q^2 - q^2\ell$ model. However, once stratification effects upon the mixing length were included using a Richardson number dependent stability function, similar solutions were obtained with both approaches. Also, other turbulence energy methods which took account of the influence of buoyancy effects yielded similar internal tides. Comparison of computed internal tides in which the eddy viscosity and diffusivity were determined using an algebraic formulation depending upon Richardson number, with those computed using the two-equation ($q^2 - q^2\ell$) turbulence energy model, did not reveal any significant differences. This comparison of a range of turbulence energy models and algebraic viscosity suggests that the simpler mixing models can produce similar internal tides to those found with the more complex models. The turbulence energy models do, however, give significantly more insight into the mechanisms producing the turbulence and its spatial variability than the algebraic eddy viscosity models, in particular the

region of enhanced mixing above the shelf break which is responsible for the cooling observed in this area [23]. Calculations also show that the differences between the internal tides computed with this range of models is small compared with differences produced by seasonal variations in the temperature field.

In earlier calculations of tides in homogeneous regions Xing and Davies [4–6] found very little difference in tidal currents computed with a range of turbulence models, however when stratification was included there were significant differences. Based upon these results, Xing and Davies [4,6,12] suggested that a rigorous validation of turbulence energy models would be the computation of tides in stratified regions, and from the results of the calculation of the internal tide using the range of turbulence models described here, this appears to be true. The major difficulty, however, is the accurate determination of the initial density field required to initialize the model. From the calculations presented in the latter part of the paper it is clear that an initial synoptic density field must be obtained with a high level of precision, together with subsequent density fields and turbulence energy measurements [43,44] in order to truly assess the predictive skill of the turbulence models [2]. Hopefully in future years the accurate and detailed measurements required to rigorously validate models of internal tide generation and associated mixing will be available.

In this paper, the sensitivity of internal tide generation to the form of parameterization of mixing and variations in density field has been examined. However, the influence of changes in topography is also important [19,17] and calculations to examine this in detail are presently in progress, and will be reported subsequently.

ACKNOWLEDGMENTS

The authors are indebted to Mr. R.A. Smith for help in finalising the figures, and to Mrs J. Hardcastle, Mrs L. Parry and Mrs L. Ravera for typing the text.

REFERENCES

1. A.M. Davies and J.E. Jones, 'Application of a three-dimensional turbulence energy model to the determination of tidal currents on the northwest European shelf', *J. Geophys. Res.*, **95**, 18143–18162 (1990).
2. A.M. Davies and J. Xing, 'An intercomparison and validation of a range of turbulence energy schemes used in three dimensional tidal models', in D.R. Lynch and A.M. Davies (eds.), *Qualitative Skill Assessment for Coastal Ocean Models*, AGU Coastal and Estuarine Series, 1995, pp. 71–96.
3. A.M. Davies and H. Gerritsen, 'An intercomparison of three dimensional tidal hydrodynamic models of the Irish Sea', *Tellus*, **46A**, 200–221 (1994).
4. J. Xing and A.M. Davies, 'Application of three dimensional turbulence energy models to the determination of tidal mixing and currents in a shallow sea', *Prog. Oceanogr.*, **35**, 153–205 (1995).
5. J. Xing and A.M. Davies, 'Application of turbulence energy models to the computation of tidal currents and mixing intensities in shelf edge regions', *J. Phys. Oceanogr.*, **26**, 417–447 (1996a).
6. J. Xing and A.M. Davies, 'Application of a range of turbulence models to the determination of M_4 tidal current profiles', *Cont. Shelf Res.*, **16**, 517–547 (1996b).
7. A.K. Blackadar, 'The vertical distribution of wind and turbulent exchange in a neutral atmosphere', *J. Geophys. Res.*, **67**, 3095–3120 (1962).
8. A.M. Davies, 'A three-dimensional model of the northwest European continental shelf with application to the M_4 tide', *J. Phys. Oceanogr.*, **16**, 797–813 (1986).
9. A.M. Davies, 'On using turbulence energy models to develop spectral viscosity models', *Cont. Shelf Res.*, **11**, 1313–1353 (1991).
10. A.M. Davies, 'A bottom boundary layer-resolving three dimensional tidal model: a sensitivity study of eddy viscosity formulation', *J. Phys. Oceanogr.*, **23** 1437–1453 (1993).
11. A.M. Davies and J. Lawrence, 'A three dimensional model of the M_4 tide in the Irish Sea: the importance of open boundary conditions and influence of wind', *JGR (Oceans)*, **99**, 16197–16227 (1994).
12. J. Xing and A.M. Davies, 'The influence of mixing length formulation and stratification upon tidal currents in shallow seas', *Estuar. Coast. Shelf Sci.*, **42**, 417–456 (1996c).

13. J. Xing and A.M. Davies, 'Formulation of a three-dimensional shelf edge model and its application to internal tide generation', *Cont. Shelf Res.*, in press (1998).
14. J. Xing and A.M. Davies, 'Processes influencing the internal tide, higher tidal harmonics, and tidally induced mixing on the Malin–Hebrides shelf', *Prog. Oceanogr.*, **38**, 155–204 (1997).
15. T.J. Sherwin, 'Evidence of a deep internal tide in the Faeroe–Shetland Channel', in B.B. Parker (ed.), *Tidal Hydrodynamics*, Wiley, New York, 1991, pp. 469–488, 883pp.
16. T.J. Sherwin and N.K. Taylor, 'Numerical investigations of linear internal tide generation in the Rockall Trough', *Deep Sea Res.*, **37**, 1595–1618 (1990).
17. P.G. Baines, 'On internal tide generation models', *Deep-Sea Res.*, **29**, 307–338 (1982).
18. P.G. Baines and X.-H. Fang, 'Internal tide generation at continental shelf/slope junction: a comparison between theory and laboratory experiments', *Dyn. Atmos. Oceans*, **2**, 297–314 (1985).
19. P.D. Craig, 'Solutions for internal tidal generation over coastal topography', *J. Marine Res.*, **45**, 83–105 (1987).
20. P.E. Holloway, 'On the dissipation of internal tides', in B.B. Parker (ed.), *Tidal Hydrodynamics*, Wiley, New York, 1991, pp. 449–468, 883pp.
21. K.G. Lamb, 'Numerical experiments of internal wave generation by strong tidal flow across a finite amplitude bank edge', *J. Geophys. Res.*, **99**, 843–864 (1994).
22. A.D. Heathershaw, A.L. New and P.D. Edwards, 'Internal tides and sediment transport at the shelf break in the Celtic Sea', *Cont. Shelf Res.*, **1**, 485–517 (1987).
23. A.L. New, 'Internal tidal mixing in the Bay of Biscay', *Deep-Sea Res.*, **35**, 691–709 (1988).
24. A.L. New and R.D. Pingree, 'Evidence for internal tidal mixing near the shelf break in the Bay of Biscay', *Deep-Sea Res.*, **37**, 1783–1803 (1990).
25. D.J. Ellett, A. Edwards and R. Bowers, 'The hydrography of the Rockall Channel—an overview', *The Oceanography of the Rockall Channel Proceedings of the Royal Society of Edinburgh 88B*, 1986.
26. B. Johns, P. Marsaleix, C. Estournel and R. Vehil, 'On the wind-driven coastal upwelling in the Gulf of Lions', *J. Marine Syst.*, **3**, 309–320 (1992).
27. R.L. Haney, 'On the pressure gradient force over steep topography in sigma coordinate ocean models', *J. Phys. Oceanogr.*, **21**, 610–619 (1991).
28. G.L. Mellor, T. Ezer and L.-Y. Oey, 'The pressure gradient conundrum of sigma coordinate ocean models', *J. Atmos. Ocean Technol.*, **11**, 1126–1134 (1994).
29. A. Beckmann and D.B. Haidvogel, 'Numerical simulation of flow around a tall isolate seamount. Part 1: Problem formulation and model accuracy', *J. Phys. Oceanogr.*, **23**, 1736–1753 (1993).
30. I.D. James, 'Advection schemes for shelf sea models', *J. Marine Syst.*, **8**, 237–254 (1995).
31. J. Xing and A.M. Davies, 'The influence of wind effects upon internal tides in shelf edge regions', *Journal of Physical Oceanography*, **27**, 2100–2125 (1997).
32. H. Baumert and G. Radach, 'Hysteresis of turbulent kinetic energy in nonrotational tidal flows: a model study', *J. Geophys. Res.*, **97**, 3669–3677 (1992).
33. J.M. Beckers, 'Application of the GHER 3D general circulation model to the western Mediterranean', *J. Marine Syst.*, **1**, 315–332 (1991).
34. A.F. Blumberg and G.L. Mellor, 'A description of a three-dimensional coastal ocean circulation model', in N.S. Heaps (ed.), *Three-Dimensional Coastal Ocean Models*, American Geophysical Union, Washington, D.C., Coastal and Estuarine Sciences, No. 4, 1987, pp. 1–16.
35. B. Galperin, L.H. Kantha, S. Hassid and A. Rosati, 'A quasi-equilibrium turbulent energy model for geophysical flows', *J. Atmos. Sci.*, **45**, 55–62 (1988).
36. B. Johns and T. Oguz, 'Turbulent energy closure schemes', in N.S. Heaps (ed.), *Three Dimensional Coastal Ocean Models*, A.G.U., 1987, pp. 17–40.
37. P.J. Luyten, E.L. Deleersnijder, J. Ozer and K.G. Ruddick, 'Presentation of a family of turbulence closure models for stratified shallow water flows and preliminary application to the Rhine outflow region', *Cont. Shelf Res.*, **16**, 101–130 (1996).
38. A.G. Davies, R.L. Soulsby and H.L. King, 'A numerical model of the combined wave and current bottom boundary layer', *J. Geophys. Res.*, **93**, 491–508 (1988).
39. A.M. Davies and J.E. Jones, 'On the numerical solution of the turbulence energy equations for wave and tidal flows', *Int. j. numer. methods fluids*, **12**, 17–41 (1991).
40. B. Johns and J. Xing, 'Three dimensional modelling of the free-surface turbulence flow of water over a bed form', *Cont. Shelf Res.*, **13**, 705–723 (1993).
41. C.E. Naimie, J.W. Loder and D.R. Lynch, 'Seasonal variation of the three-dimensional residual circulation on Georges Bank', *J. Geophys. Res.*, **99**, 15967–15989 (1994).
42. W.H. Munk and E.R. Anderson, 'Notes on a theory of the thermocline', *J. Marine Res.*, **1**, 276–295 (1948).
43. W.R. Crawford, 'Tidal mixing and nutrient flux in the waters of southwest British Columbia', in B.B. Parker (ed.), *Tidal Hydrodynamics*, Wiley, New York, 1991, pp. 855–872.
44. A.E. Gargett, 'Observing turbulence with a modified acoustic doppler current profiler', *J. Atmos. Oceanic Technol.*, **11**, 1592–1610 (1994).

